

Beneficial metabolic effects of TREM2 in obesity are uncoupled from its expression on macrophages

Omar Sharif^{1,2,3,4*}, Julia Stefanie Brunner^{1,2,3,4,12}, Ana Korosec^{1,2,13}, Rui Martins^{1,2,14}, Alexander Jais^{5,15}, Berend Snijder^{2,16}, Andrea Vogel^{3,4}, Michael Caldera⁶, Anastasiya Hladik^{1,2}, Karin Lakovits^{1,2}, Simona Saluzzo^{1,2,17}, Benedikta Boehm^{1,2}, Anna-Dorothea Gorki^{1,2}, Ildiko Mesteri⁷, Josefine Lindroos-Christensen^{5,18}, Katharina Tillmann⁸, Dagmar Stoiber^{9,10}, Jörg Menche^{2,6,11}, Gernot Schabbauer^{3,4}, Martin Bilban⁵, Giulio Superti-Furga^{2,9}, Harald Esterbauer⁵ and Sylvia Knapp^{1,2*}

¹Department of Medicine I, Laboratory of Infection Biology, Medical University of Vienna, Vienna, Austria. ²Research Center for Molecular Medicine of the Austrian Academy of Sciences, 1090 Vienna, Austria. ³Institute for Vascular Biology, Centre for Physiology and Pharmacology, Medical University Vienna, Vienna, Austria. ⁴Christian Doppler Laboratory for Arginine Metabolism in Rheumatoid Arthritis and Multiple Sclerosis, Vienna, Austria. ⁵Department of Laboratory Medicine, Medical University of Vienna, Vienna, Austria. ⁶Department of Structural and Computational Biology, Max Perutz Labs, University of Vienna, Campus Vienna Biocenter 5, A-1030 Vienna, Austria ⁷Institute of Pathology, Überlingen, Germany. ⁸Center of Biomedical Research, Medical University of Vienna, Vienna, Austria. ⁹Institute of Pharmacology, Center of Physiology and Pharmacology, Medical University of Vienna, Vienna, Austria. ¹⁰Department of Pharmacology, Physiology and Microbiology, Division Pharmacology, Karl Landsteiner University of Health Sciences, Krems, Austria. ¹¹Faculty of Mathematics, University of Vienna, Oskar-Morgenstern-Platz 1, A-1090 Vienna, Austria. ¹²Present address: Cell Biology Program, Sloan Kettering Institute, Memorial Sloan Kettering Cancer Center, New York, NY, USA.

¹³Present address: Skin, Endothelium Research Division, Department of Dermatology, Medical University of Vienna, Vienna, Austria. ¹⁴Present address: Instituto Gulbenkian de Ciência, Oeiras, Portugal. ¹⁵Present address: Helmholtz Institute for Metabolic, Obesity and Vascular Research (HI-MAG), Leipzig, Germany. ¹⁶Present address: Department of Biology, Institute of Molecular Systems Biology, ETH Zurich, Zurich, Switzerland. ¹⁷Present address: Department of Dermatology, Medical University of Vienna, Vienna Austria. ¹⁸Present address: Novo Nordisk, Søborg, Denmark.

***Correspondence:**

Omar Sharif: Omar.Sharif@meduniwien.ac.at, Tel: +43-1-40160-31108

Sylvia Knapp: Sylvia.Knapp@meduniwien.ac.at, Tel: +43-1-40400-51390

Abstract

Obesity-induced white adipose tissue (WAT) hypertrophy is associated with elevated adipose tissue macrophage (ATM) content. Overexpression of the triggering receptor expressed on myeloid cells 2 (TREM2) reportedly increases adiposity, worsening health. Paradoxically, using insulin resistance, elevated fat mass and hypercholesterolemia as hallmarks of unhealthy obesity, a recent report demonstrated ATM-expressed TREM2 promoted health. Here, we identified that in mice TREM2 deficiency aggravated diet-induced insulin resistance and hepatic steatosis independently of fat and cholesterol levels. Metabolomics linked TREM2 deficiency with elevated obesity-instigated serum ceramides that correlated with impaired insulin sensitivity. Remarkably, while inhibiting ceramide synthesis exerted no influences on TREM2-dependent ATM remodeling, inflammation or lipid load, it restored insulin tolerance, reversing adipose hypertrophy and secondary hepatic steatosis of TREM2-deficient animals. Bone marrow transplantation experiments revealed unremarkable influences of immune cell-expressed TREM2 on health instead demonstrating that WAT-intrinsic mechanisms impinging on sphingolipid metabolism dominate in TREM2's systemic protective effects on metabolic health.

Introduction

Obesity and associated metabolic disorders like insulin resistance, type 2 diabetes and hepatic steatosis constitute a major public health crisis. Obesity is characterized by excessive lipid accumulation in white adipose tissue (WAT), pathological WAT expansion, adipocyte hypertrophy and WAT immune cell infiltration, with adipose tissue macrophages (ATM) constituting a substantial fraction of this cell infiltrate (1).

ATM numbers increase through monocyte recruitment into adipose occurring partly via monocyte chemoattractant protein 1/C-C chemokine receptor type 2 (MCP-1/CCR2) (2, 3). Although in diet-induced obesity (DIO), ATMs were proposed to promote low grade adipose inflammation contributing to insulin resistance (4, 5), recent observations indicate extensive ATM heterogeneity suggesting in DIO, increases in ATM number rather than activation, may be responsible for low-grade adipose inflammation (6-8). F4/80⁺CD11b⁺CD11c⁻ (FB) ATMs represent resident macrophages while F4/80⁺CD11b⁺CD11c⁺ (FBC) ATMs represent newly recruited cells, rich in lysosomal markers that also express CD9 (4, 6, 9). Single cell RNA sequencing studies have corroborated the concept of obesity-instigated dynamic ATM remodeling and heterogeneity, further indicating CD9-expressing ATMs are circulation-derived and possess a transcriptional signature associated with lipid metabolism and phagocytosis (8, 9). Together, ATMs respond to their lipid rich environment and fulfil their main function of clearing up dying adipocytes and preventing peripheral lipid spillover that are consequences of DIO-instigated exhausted adipose expansion (1, 10, 11). Numerous studies indicate ectopic lipid storage is associated with impaired insulin signaling and resistance. Participating lipid species include various ceramides and complex sphingolipids, like glucosylceramides, lactosylceramide, sphingomyelin and sialic acid-containing glycosphingolipids such as ganglioside GM3 (12-14).

The triggering receptor on myeloid cell 2 (TREM2) regulates osteoclastogenesis and microglial responses and genetic variants of TREM2 are a risk factor for Alzheimer's disease (15-17). Consistent with studies demonstrating TREM2 binding to various lipids including sphingomyelin, phosphatidylcholine and cardiolipin (18, 19), TREM2-deficient microglia exhibit lipid metabolism defects (20). Mice globally overexpressing TREM2 exhibit impaired insulin sensitivity following caloric excess, an effect attributed to increases in body adiposity, suggesting TREM2 exerts detrimental effects on metabolic health (21). Contrastingly, a recent report demonstrated that mice globally genetically lacking TREM2 also exhibited weight gain, aggravated insulin resistance and glucose intolerance. This study assigned a critical role for immune cell-expressed TREM2 to these effects, particularly suggesting that lipid-associated TREM2 and CD9-expressing ATMs prevent DIO-instigated adipose hypertrophy and loss of metabolic homeostasis (8).

Here, we identified that during DIO, TREM2 deficiency was associated with attenuated F4/80⁺CD11b⁺CD11c⁺ (FBC) ATMs that progressively led to selective ATM loss, which coincided with accelerated secondary hepatic steatosis and sphingolipid-mediated toxicity. Bone marrow transplantation showed that although macrophage/immune cell-expressed TREM2 restrained adipose hypertrophy, this was uncoupled from TREM2's protective effects on metabolic health.

Methods

Animals

All procedures were conducted in compliance with protocols approved by the Medical University of Vienna and the Austrian Ministry of Sciences under the project number BMWF-66.009/0276-II/3b/2013.

Trem2^{-/-} mice backcrossed onto a 98% C57BL/6 background were previously described (22). Wildtype (WT) C57BL/6J and B6.SJL-*Ptprc*^a*Pepc*^b/BoyCrl (herein CD45.1) mice were purchased from Charles River (# CRL:632, CRL:494). All mice were bred at the Medical University of Vienna and housed under SPF conditions with temperatures ranging from 21-23°C in cages (5 mice per cage) with micro-isolator tops with a 12 hr light cycle (7 am - 7pm). Unless otherwise indicated, 6 week old male age matched mice were used. Dietary interventions started at 6 weeks of age using a diet that contained 60% calories of fat (high fat diet, HFD) (Research Diets, #D12492).

Human Subjects

Visceral adipose biopsies from 23 lean, 31 obese insulin-resistant (obIR) individuals (who clearly exhibited elevated insulin resistance (HOMA-IR \geq 5)) and 29 obese insulin-sensitive (obIS) individuals (who showed no signs of systemic insulin resistance, (i.e., HOMA-IR \leq 2)) were obtained under informed consent as previously described (23).

Bone-marrow Transplantation

Bone marrow transplantation was performed as previously described (24). Whole bone marrow from WT C57BL/6J and *Trem2*^{-/-} donor mice was prepared by flushing the tibia and femur with sterile RPMI. 2×10^6 cells were injected retro-orbitally into lethally irradiated (9Gy) 6 week old recipient WT and *Trem2*^{-/-} male mice under anesthesia. After a 6 week recovery period (25) during which the mice were placed on a standard chow diet (ND), mice were administered a HFD for the indicated times. As a control for chimerism some mice received CD45.1 marrow and chimerism was determined using flow cytometry. The population of CD11b⁺ CD45.1⁺ cells within the blood was >99%, demonstrating successful transplantation.

Sphingolipid Blockage during Diet Induced Obesity

Myriocin was administered as previously described with some minor modifications (26, 27). 8 weeks post diet induced obesity (DIO), mice were injected 3 x weekly with saline control or myriocin (Sigma-Aldrich, #M1177) at a dose of 0.5 mg/kg and maintained on a HFD for the indicated times.

Glucose and Insulin Tolerance tests

Following an overnight fast, mice were administered 20% glucose (1 g/kg) by oral gavage and blood samples for glucose and insulin measurements were collected from the tail vein at the indicated times. Insulin tolerance was assessed after a 2 hr fast by intraperitoneal administration of human regular insulin (0.75 U/kg). Glycemia was assessed using a Accu-Check glucometer in combination with Accu Check Go Test Strips (Roche, #05182913). Following insulin tolerance tests, mice were allowed to recover for 4-6 days after which oral glucose tolerance was measured.

Statistical Analysis

Data are expressed as mean \pm SEM. Statistical significance in two-group comparisons was assessed with an unpaired Student's t test. When indicated, a Mann-Whitney U test was used for analysis of nonparametric data. ITT and oGTT data were analysed using a two-way ANOVA followed by Bonferroni post-test with both time and group as sources of variation. For multivariable comparisons, we performed a one-way ANOVA followed by Tukeys multiple comparison test. Results were analyzed with Graph Pad Prism software version 8, and a $p < 0.05$ was regarded as statistically significant.

Data and Resource Availability

The data sets generated and analyzed during this study are available from the corresponding authors upon reasonable request.

Additional methods are described in the supplementary material

Results

TREM2 is upregulated in visceral adipose during obesity in mice and man.

To explore the role of TREM2 during DIO we first fed C57BL/6J mice a 60% high fat diet (HFD) for 13 weeks and observed elevated *Trem2* in heart, kidney and liver relative to animals fed a normal chow diet (ND) (Figure. 1A). Notably, *Trem2* expression increased in all tested “metabolically unhealthy” mouse visceral WAT depots as opposed to “healthy” subcutaneous fat (Figure. 1B) (28, 29). To examine if DIO impacted *Trem2* expression on infiltrating FBC ATMs (4, 5) or mature adipocytes (MA), we isolated both MA and the stromal vascular fraction (SVF) from the epididymal white adipose (eWAT) of HFD fed animals and subsequently positively selected the SVF for CD11c⁺ cells and examined *Trem2* levels in both cell types. While F4/80 and adiponectin were selectively expressed on ATMs or MAs respectively, *Trem2* was detected on both cell types (Figure. 1C). Immunohistochemistry confirmed strong TREM2 expression within inflammatory “crown-like” structures that were clearly increased during DIO (Figure. 1D). To test if increases in obesity-induced visceral adipose *Trem2* expression were conserved, we measured *Trem2* levels in a previously published cohort of clinically obese (BMI>30) and age matched obese insulin-resistant (obIR - HOMA-IR \geq 5), obese insulin-sensitive (obIS-HOMA-IR \leq 2) and lean individuals (23). *Trem2* was elevated in the visceral adipose of obese insulin-resistant versus obese insulin-sensitive and lean humans (Figure. 1E). Thus, DIO results in conserved increases in *Trem2* expression within the visceral adipose of mice and man, and is associated with insulin resistance.

Loss of TREM2 aggravates metabolic disease.

To address the role of TREM2 in metabolic disease we fed *Trem2*^{-/-} mice a HFD for 13 weeks and assessed their metabolic health compared to WT C57BL/6J controls. *Trem2*^{-/-} mice clearly exhibited impaired insulin sensitivity and glucose tolerance (Figure. 2A-C). These effects were independent of weight and there were no differences in fat mass in both the subcutaneous and visceral depots between genotypes (Figure. 2D and 2E). Time course experiments in independent cohorts of mice corroborated no differences in weight gain between genotypes, showing that *Trem2*^{-/-} animals became insulin insensitive versus controls eight weeks post HFD, which progressively worsened over time (Supplemental Figure. 1A, 1B). Importantly, *Trem2*^{-/-} mice exhibited normal insulin tolerance relative to WT animals in the naïve and normal chow diet (ND) state, demonstrating metabolic stress induced by HFD feeding was required for TREM2 to influence metabolic health (Supplemental Figure. 1A). Considering single cell RNA sequencing studies imply the TREM2 pathway represents a conserved macrophage response for the detection of pathogenic lipids across multiple tissues (8) and an interrelationship between insulin resistance and Alzheimer's disease is suggested (30) of which TREM2 genetic variants are a risk factor (17), we next let both genotypes age to one year and examined insulin tolerance. These experiments confirmed the unremarkable effects of TREM2 on insulin sensitivity in the context of ND, even upon aging (Supplemental Figure. 1C and 1D). The decreased insulin sensitivity of *Trem2*^{-/-} animals post 13 weeks HFD was independent of changes in serum cholesterol and triglycerides (Supplemental Figure. 2A). In line, we observed no differences in liver triglycerides, steatosis and serum indicators of hepatotoxicity including alanine transaminase (ALT) and aspartate transaminase (AST) 13 weeks post HFD (Supplemental Figure. 2B-D). To shed light on the physiological mechanisms whereby TREM2 impacted insulin resistance, we next performed indirect calorimetry on weight-matched obese mice but did not observe differences in energy

expenditure or activity between genotypes (Figure. 2F-H). Together, these data largely support recent findings indicating that in DIO-instigated insulin resistance TREM2 exerts protective effects (8, 21). However, given that global over-expression of TREM2 (21) as well as TREM2 deficiency (8) was reported to promote weight gain upon HFD, our data indicate that loss of metabolic homeostasis in obese TREM2 deficient mice did not correlate with increases in fat mass.

Elevated adipose hypertrophy in obese TREM2 deficient animals is associated with remodeling of ATM populations.

We next monitored visceral adipose hypertrophy in both sets of obese animals. The eWAT of *Trem2*^{-/-} mice contained larger hypertrophic adipocytes versus controls, suggesting TREM2 prevented pathological adipose expansion during HFD feeding (Figure. 3A and 3B). Pathological WAT expansion of obese mice is associated with WAT hypoxia and activation of the oxygen sensitive transcription factor hypoxia inducible factor 1 (HIF-1 α), which heterodimerizes with HIF-1 β , to activate hypoxia related transcription (1, 31). Evaluating eWAT transcript levels of *Hif-1 α* , *Hif-1 β* and other well established components of the hypoxia pathway (31) demonstrated unremarkable differences between HFD-fed genotypes (Supplemental Figure. 3A). Further, pro-apoptotic *Bax* was unaltered and anti-apoptotic *Bcl-2* levels were elevated, respectively, in hypertrophic *Trem2*^{-/-} eWAT, suggesting that the elevated hypertrophy was not associated with augmented apoptosis (Supplemental Figure. 3A). Confirmatory and consistent with published observations indicating that significant adipocyte apoptosis in eWAT peaks between 16-20 weeks of HFD feeding (32), we could not detect any active caspase 3 in 13 week HFD fed animals (Supplemental Figure. 3B and 3C). Together these observations suggest that the larger

hypertrophic adipocytes of *Trem2*^{-/-} animals are disconnected from elevated hypoxia and apoptosis.

We next examined whether there were differences in visceral eWAT ATM profiles between obese genotypes. Circulation-derived FBC ATMs comprise the majority of increased ATM content in obesity (4, 6, 33). CD206 is a marker for alternatively activated ATMs that is also robustly expressed by FB (CD11c⁻) ATMs in the lean state (34). Monitoring visceral ATM content, demonstrated that while obesity was associated with marked overall ATM expansion and recruitment, there were no differences between genotypes (Figure. 3C and 3D). Consistent with reports that DIO instigated preferential increases in FBC over FB ATMs (4, 6, 33), HFD feeding led to a shift in ATM populations, with an increased ratio of FBCs versus CD206 expressing FBs, that was dramatically attenuated upon TREM2 deficiency (Figure. 3E and Supplemental Figure. 4A). Indeed, the ATM compartment of obese *Trem2*^{-/-} mice exhibited substantial remodeling with decreased FBCs and elevated levels of CD206 expressing FBs and FBCs versus control animals (Figure. 3F and 3G). Altogether, these data suggest that although the aggravated metabolic disease upon loss of TREM2 is associated with augmented adipocyte hypertrophy, the ATM signature within this hypertrophic adipose is skewed, incompletely advancing to the HFD state observed in controls.

Protective effects of TREM2 on metabolic health in obesity are linked to sphingolipids.

We next used mass spectrometry to determine which metabolic stressors were associated with the aggravated insulin resistance of *Trem2*^{-/-} animals. We quantified 429 serum metabolites including various lipid species like sphingolipids, sphingomyelin (SM), acylcarnitines and

glycerophospholipids in both sets of animals under both dietary conditions. We chose these metabolites as they are associated with insulin resistance (13, 35-37), and glycerophospholipids including phosphatidylcholines (PC), phosphatidylglycerols (PG) are reported to activate TREM2 signaling (19). Targeted metabolomics of serum from control and *Trem2*^{-/-} mice on a ND or HFD for 14 weeks indicated that the metabolic effect of TREM2 deficiency was similar to that of HFD feeding (correlation of significantly altered metabolites is 0.56, $p < 2 \times 10^{-11}$) and that long chain ceramides (C16:0, C18:0, C20:0), selected acylcarnitines (C18:0, C18:1, C18:2), and sphingomyelin (C22:3) were significantly upregulated following both HFD feeding and TREM2 ablation (Figure. 4A). Systematically comparing metabolite levels in mice with low and high glucose levels upon 45 min of insulin treatment, revealed gradual and stepwise relationships between the relative abundance of these same metabolites and insulin resistance, with levels of ceramides (C16:0, C18:0, C20:0) and sphingomyelin (C22:3) being highest in HFD-fed *Trem2*^{-/-} mice (Figure. 4B and Supplemental Figure. 5A). Correlations between abundance of these metabolites and glycemia were rapid and evident 15 min post-insulin treatment (Supplemental Figure. 5B). As ceramides are potent lipotoxic mediators in obesity, which attenuate insulin signaling in part by inactivating the kinase AKT (12, 38), we assessed hepatic AKT activity after intraperitoneal administration of insulin to both groups of HFD-fed animals. Loss of TREM2 was associated with substantially decreased insulin-stimulated liver AKT phosphorylation, indicating that following 13 weeks of HFD feeding, TREM2 deficiency elicited body wide changes in insulin sensitivity and that sphingolipids might be causally linked (Figure. 4C).

To demonstrate that altered sphingolipid metabolism was crucial to the insulin resistance of metabolically stressed *Trem2*^{-/-} animals, we next blocked sphingolipid synthesis at a time post-DIO when *Trem2*^{-/-} animals first become insulin resistant versus controls, i.e. 8 weeks following

HFD (Supplemental Figure. 1A) and subsequently examined animals post-DIO (Figure. 4D). We treated both genotypes with myriocin, a specific inhibitor of serine palmitoyl-transferase (SPT), the rate limiting enzyme of *de novo* ceramide synthesis that converts palmitoyl-CoA and serine into ceramides (12, 26, 27). Targeted serum metabolomics reproduced that long chain ceramides (C16:0-C24:0), were particularly upregulated by the HFD feeding regimen (Supplemental Figure. S6A). Notably, in both genotypes, myriocin treatment during HFD feeding led to an upregulation in short-chain ceramides (<C16:0) and downregulation of long and ultra-long ceramides (>C16:0), an effect that was particularly prominent in TREM-2 deficient animals (Supplemental Figure. S6B). Short chain ceramides upregulated by myriocin in both genotypes included C10:0, C15:0, while long and ultra-long ceramides downregulated included C22:1, C24:0. Ceramides particularly impacted by myriocin in *Trem2*^{-/-} animals included C18:0, C21:0 and C25:1 (Figure 4E). Together, these data indicated that myriocin negatively impacts the serum levels of metabolically detrimental long and ultra-long chain ceramide species (26, 36, 39), suggesting it might improve insulin sensitivity. Indeed, *Trem2*^{-/-} animals treated with saline control were insulin resistant compared to WT mice, and myriocin treatment completely reversed this impaired insulin sensitivity, with both effects independent of weight (Figure. 4F and 4G). Further, myriocin treatment of *Trem2*^{-/-} animals decreased metabolic stress induced adipocyte enlargement to levels of control animals, demonstrating the contribution of sphingolipids to visceral adipose morphology and expansion (Figure. 4H and 4I). These data assign a strong contribution of metabolic stress induced sphingolipid and long chained ceramide synthesis (>C16:0) to the elevated insulin resistance and adipose hypertrophy of TREM2 deficient animals.

We next examined the impact of myriocin treatment on ATM numbers, remodeling and inflammation. Sphingolipid blockage exerted both unremarkable effects on ATM content and

remodeling as obese *Trem2*^{-/-} animals treated with myriocin still exhibited decreased FBCs and elevated levels of CD206 expressing FBs compared to control mice (Figure. 5A-C). To evaluate impacts of myriocin on ATM inflammation within the eWAT of both obese genotypes 13 weeks post HFD, using F4/80 and CD11b antibodies we flow-assisted cell sorted a pool FB-ATMs that express CD11c or CD206 or both markers (Supplemental Figure 4A). Consistent with the incomplete ATM remodeling of *Trem2*^{-/-} animals, versus controls, reproducibly elevated expression of canonical markers of alternative macrophage (M2) activation, *Fizz1* and *Ym1* (40) was apparent in *Trem2*^{-/-} ATMs isolated from different obese animals (Figure. 5D). However, suggesting TREM2 does not alter ATM mediated inflammation, there were no reproducible decreases in markers of classical M1 activation (*iNOS*) (40), nor differences in pro-inflammatory cytokine expression between ATM genotypes. Importantly, sphingolipid blockage exerted no influences herein (Figure 5D).

Since lipid associated TREM2-expressing ATMs were recently reported to prevent DIO-instigated adipose hypertrophy and loss of metabolic homeostasis (8), in the same cohort of animals, we evaluated impacts of TREM2 on ATM mediated lipid uptake and the effects of myriocin herein. Although, as previously observed, there were no differences in overall ATM expansion between genotypes, BODIPY staining revealed less lipid laden *Trem2*^{-/-} ATMs, confirming published data that ATM expressed TREM2 is associated with lipid uptake in obesity (8) (Figure. 5E-F and Figure 3D). While there was a slight tendency ($p=0.0892$), that myriocin treatment increased the attenuated lipid load of *Trem2*^{-/-} ATMs, this was not statistically significant.

Collectively, these data suggest that the effects of sphingolipids on adipose hypertrophy and metabolic health are uncoupled from TREM2 dependent shifts in ATM remodeling, inflammation and lipid load.

TREM2 exerts protective effects in secondary liver steatosis that are associated with specific defects in ATM content and sphingolipids.

Insulin resistance is often accompanied by hepatic steatosis. As *Trem2*^{-/-} mice were more insulin resistant compared to controls 13-14 weeks post-DIO, despite no differences in hepatic steatosis (Figure. 2, Figure. 4 and Supplemental Figure. 2), we next hypothesized that prolonged HFD feeding might unleash a secondary steatotic phenotype in these animals. An extended 26 weeks HFD regime led to striking insulin resistance with liver morphology and scoring of liver steatosis by an experienced pathologist indicating that *Trem2*^{-/-} animals exhibited larger and more steatotic livers, as opposed to controls (Figure. 6A-C). Further, akin to 13 weeks of HFD feeding (Figure. 3E), prolonged obesity was associated with a decreased ratio of FBCs versus CD206 expressing FBs (Figure. 6D). Suggestive that decreased circulation-derived FBCs upon TREM2 deficiency impacted ATM content during prolonged 26 weeks HFD feeding, compared to controls the visceral adipose of TREM2 deficient animals exhibited ATM loss (Figure. 6E and 6F). These lower macrophage numbers were specific for fat macrophages and independent of differences in circulating or inflammatory monocytes as there were no differences in hepatic macrophage content or white blood cell counts between obese genotypes (Supplemental Figure. 4B-E and Figure. 6G). Hypothesizing that upon prolonged HFD feeding, attenuated chemotactic signals for ATM recruitment and expansion within the visceral adipose environment of TREM2 deficient animals might be responsible, we next prepared mature adipocytes from both sets of obese genotypes and generated adipocyte conditioned media (ACM). Despite comparable protein content in both genotypes, ACM derived from adipocytes collected from 26 week HFD-fed TREM2 deficient animals exhibited significantly reduced MCP-1 amounts, that in turn generated lower migratory responses of macrophages compared to ACM from 26 week HFD-fed control animals (Figure. 6H-

I). Together, these data indicate that signals derived from the adipose environment contribute to ATM content. This observation is consistent with adipocytes being significant sources of MCP-1 (2), and suggest influences of TREM2 herein.

As metabolic stress-induced sphingolipid synthesis was critical for the elevated insulin resistance of TREM2-deficient animals, we next hypothesized that inhibition of *de novo* ceramide synthesis might reverse the enhanced hepatic steatosis of these animals. Histology and liver morphology revealed that sphingolipid blockage during prolonged 26 weeks HFD feeding ameliorated the accelerated secondary hepatic steatosis of *Trem2*^{-/-} animals to control levels (Figure. 6J and 6K). These data firmly place metabolic stress induced sphingolipid synthesis at the crux of TREM2's protective effects during metabolic health.

Non-hematopoietic expressed TREM2 influences metabolic health.

To unveil the contribution of TREM2 expressed on hematopoietic versus non-hematopoietic cells to the insulin resistance of *Trem2*^{-/-} mice, we next performed bone marrow (BM) transplantation to generate 4 groups of mice; WT, *Trem2*^{-/-} or chimeric mice - WT mice with *Trem2*^{-/-} BM (*Trem2*^{-/-}>WT) and *Trem2*^{-/-} mice transplanted with WT BM (WT>*Trem2*^{-/-}) (Figure. 7A). Surprisingly, following 13 weeks of HFD, *Trem2*^{-/-} recipient mice transplanted with either genotype of BM displayed more pronounced insulin resistance and glucose intolerance compared to WT or WT chimeric (*Trem2*^{-/-}>WT) controls (Figure. 7B-E). Examining insulin tolerance 26 weeks post HFD feeding confirmed these effects demonstrating they were independent of weight differences (Supplemental Figure. 7A and 7B). Together, these data demonstrate a major contribution of non-hematopoietic expressed TREM2 to metabolic health.

Evaluating TREM2 and F4/80 levels in eWAT, visualizing F4/80 using alkaline phosphatase together with permanent red chromogen and TREM2 with horseradish peroxidase (HRP) coupled to diaminobenzidine as a substrate, resulting in brown color, revealed significant co-localization in WT > WT animals. While both genotypes transplanted with *Trem2*^{-/-} BM (*Trem2*^{-/-}>WT or *Trem2*^{-/-}> *Trem2*^{-/-}) exhibited only red color in the “crown-like” structures, *Trem2*^{-/-} animals transplanted with WT BM, displayed brownish color, with some areas of co-localization. These data confirm TREM2 loss in ATMs in animals transplanted with *Trem2*^{-/-} BM and are consistent with data showing that the majority of ATMs in obesity are circulation derived (8, 33, 41). Examining eWAT F4/80 transcript levels revealed decreased levels in *Trem2*^{-/-} recipient mice transplanted with either genotype of BM compared to WT control mice (WT>WT), supporting our observations that chemotactic signals leading to ATMs recruitment and expansion were attenuated within visceral adipose upon TREM2 deficiency (Supplemental Figure. 8A, Figure. 6H-I). More definitive evidence was provided by experiments where we transplanted WT CD45.1 BM into both WT and *Trem2*^{-/-} animals and evaluated blood monocyte and ATM levels using flow cytometry. While both genotypes of animals exhibited a similar reconstitution of CD45.1 derived blood monocytes post 26 weeks HFD, the frequency of circulation-derived CD45.1 ATMs were significantly lower in TREM2 deficient mice (Supplemental Figure. 8B-D). Together, these data confirm the importance of signals derived from the visceral adipose of obese animals and a role for TREM2 in governing ATM content.

Importantly, while transplantation of WT mice with *Trem2*^{-/-} BM (*Trem2*^{-/-}>WT) exerted no effects on metabolic disease, it significantly increased adipose hypertrophy (Figure. 7F and 7G). A more pronounced effect was observed upon transplantation of WT BM in *Trem2*^{-/-} mice (WT>*Trem2*^{-/-}), which despite exerting unremarkable effects on metabolic health, were completely

able to reverse the elevated adipose hypertrophy of TREM2 deficient animals (Figure. 7F and 7G). Thus, although in obesity hematopoietic/macrophage expressed TREM2 restrains adipose hypertrophy, it exerts no influences on metabolic health.

The elevated hepatic steatosis of TREM-2 deficient animals is linked to visceral adipose tissue derived ceramide lipotoxicity

We next examined the cell type-specific contributions of TREM2 to hepatic steatosis. Importantly, the metabolic improvements elicited by non-hematopoietic expressed TREM2 were systemic. Both liver morphology and scoring of liver steatosis revealed more severe steatosis in *Trem2*^{-/-} recipient animals, regardless of genotype of transplanted BM, compared to WT recipient mice (Figure. 8A-B). These effects were confirmed by increased oil red O staining and elevated serum hepatotoxicity markers in *Trem2*^{-/-} recipient mice (Figure. 8A and C) and were independent of changes in serum triglyceride and cholesterol levels (Supplemental Figure. 7C and 7D). Interestingly, assessing eWAT architecture using whole mount microscopy and BODIPY labelling following prolonged HFD feeding revealed uniform staining of lipid droplets in adipose of WT mice, while in both groups of *Trem2*^{-/-} recipient mice, adipose architecture was markedly different, with areas displaying more intense staining (Figure. 8A). Noting this and that the elevated hepatic steatosis of *Trem2*^{-/-} animals was linked to ceramide levels (Fig. 6J-K), we next evaluated visceral eWAT adipose ceramide levels in the HFD-fed BMT animals. Remarkably, compared to WT recipient mice, diverse short and long chained ceramide species were reproducibly elevated in the eWAT of *Trem2*^{-/-} recipient animals, regardless of genotype of transplanted BM (Figure. 8D and Supplemental Figure. 9).

As adipose tissue is a significant ceramide source impacting hepatic steatosis during HFD feeding (39, 40), using immunohistochemistry with a ceramide detecting antibody that does not cross-react with sphingomyelin, cholesterol or other phospholipids, we next evaluated hepatic ceramide levels. Consistent, with elevated ceramide eWAT presence, *Trem2*^{-/-} recipient animals displayed augmented hepatic ceramide levels, interestingly particularly prominently in steatotic and ballooned hepatocytes (Figure. 8A). Thus prolonged obesity in TREM2 deficient mice is associated with lipotoxic effects that are linked to elevated visceral adipose ceramide production.

To further examine potential contributions of TREM2 to adipose derived signals and systemic metabolism, we next asked if the elevated sphingolipid and long chain ceramide species present in serum of HFD-fed *Trem2*^{-/-} mice versus WT controls (Figure. 4 and Supplemental Fig. 6A), were linked to adiponectin levels, which exerts its beneficial metabolic effects through sphingolipid metabolism and catabolism of cellular ceramide (42). In line with the contributions of non-hematopoietic expressed TREM2 to metabolic health, and the elevated ceramide species found in eWAT of *Trem2*^{-/-} animals, we found decreased adiponectin levels in *Trem2*^{-/-} recipient mice transplanted with either genotype of BM (Figure. 8E). These data further strengthen the importance of non-hematopoietic TREM2 in protecting against insulin resistance and hepatic steatosis, supporting the notion that adipose tissue derived signals might be responsible for the aggravated metabolic disease and ceramide instigated lipotoxicity of TREM2 deficient animals.

Discussion

Here, we show that during obesity *Trem2* expression increases in unhealthy visceral adipose in mice and man (28, 29) and in humans augmented *Trem2* was highest in obese and insulin resistant individuals, indicating this receptors' importance in metabolic health. Although elevated visceral adipose *Trem2* in obesity is likely due to increases in ATM content (4, 33), in contrast to a recent report demonstrating a crucial role for immune cell expressed TREM2 in protecting against insulin resistance and glucose intolerance (8), the bone marrow transplantation experiments herein argue that hematopoietic-expressed TREM2 is dispensable for these obesity-triggered health complications. In contrast to the aforementioned report, we further demonstrate that the aggravated metabolic disease of TREM2 deficient animals is not associated with hematopoietic cell-expressed TREM2 instigated increases in cholesterol and body adiposity (8). Moreover, we show that lipotoxic signals triggered by HFD feeding arising from metabolically stressed TREM2 deficient adipose are sufficient to exacerbate metabolic disease, independent of macrophage and adipose mass influence(s).

Obesity-instigated adipose hypertrophy is associated with both adipocyte death and increases in ATMs that are proposed to phagocytose dying adipocytes in crown like structures and scavenge residual lipid droplets (1, 10, 11). Recent work utilizing single cell RNA sequencing demonstrated TREM2 was required for the formation of lipid-associated macrophage (LAM) cell-rich crown-like structures and assigned LAMs as CD9⁺CD63⁺TREM2⁺ cells, rich in lysosomal markers exhibiting a transcriptional signature associated with lipid metabolism and phagocytosis (8). Other work showed that CD9 expressing ATMs also express CD11c and assigned a critical function for FBCs that are circulation derived, in lipid metabolism (4, 6, 9). Although we could not reproduce data demonstrating a protective effect for hematopoietic expressed TREM2 in metabolic disease,

consistent with observations that LAM accumulation is substantially reduced in HFD fed *Trem2*^{-/-} mice (8), we could demonstrate decreased FBCs upon TREM2 deficiency in obesity. Notably, as transplantation of WT mice with *Trem2*^{-/-} BM significantly increased adipose hypertrophy, we could directly demonstrate that in obesity hematopoietic/likely macrophage-expressed TREM2 regulates adipose hypertrophy. In this regard, it is notable that multiple studies focusing on the brain where TREM2 is an established player have demonstrated its critical role in the uptake of apoptotic cells and amyloid plaques (43). Although in obesity ATM expressed TREM2 might be important for the uptake of dying adipocytes, depletion of CD206 expressing ATMs attenuates adipose hypertrophy by increasing adipocyte progenitor proliferation and differentiation (44), suggesting potential involvement of shifts towards increased CD206 expression in eWAT of WT animals transplanted with *Trem2*^{-/-} BM. However, our data indicate decreases in ATM amounts stemming from circulation-derived FBCs in obese TREM2 deficient mice *per se* likely play a more important role in the elevated adipose hypertrophy of these animals. Concordantly, transplantation of *Trem2*^{-/-} mice with WT BM could completely reverse the elevated hypertrophy of HFD fed *Trem2*^{-/-} animals. Interestingly, HFD fed *Trem2*^{-/-} mice transplanted with *Trem2*^{-/-} BM displayed the most adipose hypertrophy, suggesting additional requirements for TREM-2 expression on adipocytes, where it is described to be important for adipocyte differentiation (21). The exact functions and interplay of TREM2 expression on adipose versus macrophages in the hypertrophy phenotype will be interesting areas for future investigation.

Notably, TREM2 only impacted insulin sensitivity following HFD feeding. TREM2-deficient mice fed a ND or aged mice lacking TREM2 in the context of ND feeding exhibited unremarkable differences in insulin sensitivity relative to controls, indicating that a trigger is required for TREM2 to confer a health benefit in obesity. Herein, both HFD feeding and TREM2 deficiency exhibited

commonalities on dyslipidemia with both increasing serum levels of long chain ceramides. Cellular ceramide is formed in various ways (12), and reducing the condensation of serine with palmitoyl-CoA and hence production of 3-ketosphinganine during metabolic stress, using myriocin (12, 26, 27) abolished all detrimental effects of TREM2 deficiency in obesity, indicating *de novo* ceramide production is connected to TREM2's influence. These effects were independent of body adiposity, but connected to adipose ceramide production. Accordingly, independent of weight, depletion of ceramides via transgenic overexpression of acid ceramidase in adipose of obese animals causes decreased systemic ceramide levels and improved insulin sensitivity (45). Lowering adipose ceramides by genetically targeting adipose-specific *Sptlc2* or via overexpression of adipose specific acid ceramidase in obese animals also improves hepatic steatosis implying that adipose and liver shuttle sphingolipids or that both tissues function as sinks for circulating ceramides during HFD feeding (45, 46). Our data are consistent with an adipose-liver sphingolipid cross-talk hypothesis and demonstrate the contribution of TREM2 therein. In line, early in obesity opposed to controls, *Trem2*^{-/-} animals exhibited no differences in hepatic steatosis, yet pronounced decreases in insulin-stimulated liver AKT phosphorylation, that correlated with adipose hypertrophy and increased systemic long chain ceramides that inhibit insulin signaling (26, 36). Prolonged HFD feeding of TREM2-deficient animals caused extensive hepatic steatosis connected to elevated hepatic ceramide presence, that coincided with visceral adipose ceramide production and dysfunction, indicating ceramides stored within adipose were spilled into the circulation and deposited in the liver. Decreasing *de novo* ceramide synthesis in TREM2-deficient animals reversed their elevated hepatic steatosis to control levels, which was preceded in timing by attenuated adipose hypertrophy during HFD feeding. However, decreasing *de novo* ceramide

synthesis exerted no influence on the ATM remodeling, observed in TREM2 deficient animals, indicating that these two phenomena are uncoupled.

Further, there were no effects of sphingolipid blockage on ATM mediated inflammation, which did not differ between HFD-fed genotypes, indicating that the incomplete ATM remodeling of TREM2-deficient animals early in obesity, does not impact classical M1 ATM activation. Consistent, ATMs, especially F4/80 or CD9 expressing ATMs are described to adopt a unique metabolically activated phenotype, that is not classically M1, in response to their lipid rich environment (6, 7). In this regard, although sphingolipid blockage did not statistically increase the reduced lipid load in ATMs of obese *Trem2*^{-/-} animals, there was a tendency, suggesting an involvement for WAT derived lipids and ceramides in the attenuated neutral lipid content of ATMs from obese *Trem2*^{-/-} animals.

While our study does not support a role for TREM2 expression on macrophages being related to its beneficial metabolic effects in obesity, it strongly suggests TREM2's effects on metabolic disease are linked to sphingolipid homeostasis and metabolic stress within adipose. Nonetheless, we acknowledge the limitations. Firstly, the exact contribution of TREM2 expression on mature adipocytes to metabolic health would require conditional loss of function approaches. The TREM2 deficient animals utilized in this study and those by Jaitin and colleagues, which demonstrated a protective role of immune cell expressed in metabolic health primarily through bone marrow transplantation, possess a deletion in a portion of the transmembrane and cytoplasmic domains encoded by exons 3 and 4 of *Trem2* (8, 22). To our knowledge no conditional TREM2 mouse exists possessing *loxP* sites targeting *Trem2* at this region. Moving forward, generating these animals and crossing them to mice expressing the Cre-recombinase under the adiponectin promoter would be important. Secondly, although akin to Jaitin and colleagues, versus controls we

could demonstrate incomplete ATM remodelling within TREM2 deficient hypertrophic adipose as well as decreased insulin sensitivity and glucose tolerance, contrasting results between bone marrow transplantation studies with TREM2 deficient bone marrow (8), might be impacted by differences in microbiota and mouse house specific facility factors.

Ending hypothetically, more than 25 years ago, the bone cysts in human TREM2 deficiency (Nasu Hakola disease) were described to consist of membranous and lamellar structures composed of phospholipids and triglycerides (47). Further, some disease cases exhibited sphingolipid species within their brain cortex and white matter like C16:0 and C18:0 fatty acid sulfatides, cerebroside and gangliosides (48). More recently, TREM2 binding to various lipids was demonstrated (18, 19). TREM2-deficient microglia exhibit lipid metabolism defects (20), providing a mechanistic explanation for why rare variants of TREM2 promote Alzheimer's disease (17), which intriguingly is thought to be a form of brain insulin resistance, coined type 3 diabetes (30). Together with our data, these published observations hint to the intriguing possibility that by sensing nutrients and binding elevated adipose-derived or circulating sphingolipids during obesity, TREM2 and possibly adipose-specific TREM2 may act as sink, promoting healthy function during nutrient excess. Our work also suggests that examining the interplay between TREM2, sphingolipid synthesis and brain insulin resistance in the context of Alzheimer's disease models might uncover hidden secrets on how TREM2 impacts late onset dementia.

References

1. Rutkowski JM, Stern JH, and Scherer PE. The cell biology of fat expansion. *J Cell Biol.* 2015;208(5):501-12.
2. Kanda H, Tateya S, Tamori Y, Kotani K, Hiasa K, Kitazawa R, et al. MCP-1 contributes to macrophage infiltration into adipose tissue, insulin resistance, and hepatic steatosis in obesity. *J Clin Invest.* 2006;116(6):1494-505.
3. Kamei N, Tobe K, Suzuki R, Ohsugi M, Watanabe T, Kubota N, et al. Overexpression of monocyte chemoattractant protein-1 in adipose tissues causes macrophage recruitment and insulin resistance. *J Biol Chem.* 2006;281(36):26602-14.
4. Lumeng CN, Bodzin JL, and Saltiel AR. Obesity induces a phenotypic switch in adipose tissue macrophage polarization. *J Clin Invest.* 2007;117(1):175-84.
5. Patsouris D, Li PP, Thapar D, Chapman J, Olefsky JM, and Neels JG. Ablation of CD11c-positive cells normalizes insulin sensitivity in obese insulin resistant animals. *Cell Metab.* 2008;8(4):301-9.
6. Xu X, Grijalva A, Skowronski A, van Eijk M, Serlie MJ, and Ferrante AW, Jr. Obesity activates a program of lysosomal-dependent lipid metabolism in adipose tissue macrophages independently of classic activation. *Cell Metab.* 2013;18(6):816-30.
7. Kratz M, Coats BR, Hisert KB, Hagman D, Mutskov V, Peris E, et al. Metabolic dysfunction drives a mechanistically distinct proinflammatory phenotype in adipose tissue macrophages. *Cell Metab.* 2014;20(4):614-25.
8. Jaitin DA, Adlung L, Thaïss CA, Weiner A, Li B, Descamps H, et al. Lipid-Associated Macrophages Control Metabolic Homeostasis in a Trem2-Dependent Manner. *Cell.* 2019;178(3):686-98 e14.
9. Hill DA, Lim HW, Kim YH, Ho WY, Foong YH, Nelson VL, et al. Distinct macrophage populations direct inflammatory versus physiological changes in adipose tissue. *Proc Natl Acad Sci U S A.* 2018;115(22):E5096-E105.
10. Coats BR, Schoenfelt KQ, Barbosa-Lorenzi VC, Peris E, Cui C, Hoffman A, et al. Metabolically Activated Adipose Tissue Macrophages Perform Detrimental and Beneficial Functions during Diet-Induced Obesity. *Cell Rep.* 2017;20(13):3149-61.
11. Cinti S, Mitchell G, Barbatelli G, Murano I, Ceresi E, Faloia E, et al. Adipocyte death defines macrophage localization and function in adipose tissue of obese mice and humans. *J Lipid Res.* 2005;46(11):2347-55.
12. Chavez JA, and Summers SA. A Ceramide-Centric View of Insulin Resistance. *Cell Metabolism.* 2012;15(5):585-94.
13. Haus JM, Kashyap SR, Kasumov T, Zhang R, Kelly KR, Defronzo RA, et al. Plasma ceramides are elevated in obese subjects with type 2 diabetes and correlate with the severity of insulin resistance. *Diabetes.* 2009;58(2):337-43.
14. Yamashita T, Hashiramoto A, Haluzik M, Mizukami H, Beck S, Norton A, et al. Enhanced insulin sensitivity in mice lacking ganglioside GM3. *P Natl Acad Sci USA.* 2003;100(6):3445-9.
15. Ulland TK, and Colonna M. TREM2-a key player in microglial biology and Alzheimer disease. *Nat Rev Neurol.* 2018;14(11):667-75.
16. Sharif O, and Knapp S. From expression to signaling: Roles of TREM-1 and TREM-2 in innate immunity and bacterial infection. *Immunobiology.* 2008;213(9-10):701-13.

17. Guerreiro R, Wojtas A, Bras J, Carrasquillo M, Rogaeva E, Majounie E, et al. TREM2 Variants in Alzheimer's Disease. *New Engl J Med*. 2013;368(2):117-27.
18. Cannon JP, O'Driscoll M, and Litman GW. Specific lipid recognition is a general feature of CD300 and TREM molecules. *Immunogenetics*. 2012;64(1):39-47.
19. Wang YM, Cella M, Mallinson K, Ulrich JD, Young KL, Robinette ML, et al. TREM2 Lipid Sensing Sustains the Microglial Response in an Alzheimer's Disease Model. *Cell*. 2015;160(6):1061-71.
20. Ulland TK, Song WM, Huang SCC, Ulrich JD, Sergushichev A, Beatty WL, et al. TREM2 Maintains Microglial Metabolic Fitness in Alzheimer's Disease. *Cell*. 2017;170(4):649-+.
21. Park M, Yi JW, Kim EM, Yoon IJ, Lee EH, Lee HY, et al. Triggering Receptor Expressed on Myeloid Cells 2 (TREM2) Promotes Adipogenesis and Diet-Induced Obesity. *Diabetes*. 2015;64(1):117-27.
22. Turnbull IR, Gilfillan S, Cella M, Aoshi T, Miller M, Piccio L, et al. Cutting edge: TREM-2 attenuates macrophage activation. *J Immunol*. 2006;177(6):3520-4.
23. Jais A, Einwallner E, Sharif O, Gossens K, Lu TTH, Soyol SM, et al. Heme Oxygenase-1 Drives Metaflammation and Insulin Resistance in Mouse and Man. *Cell*. 2014;158(1):25-40.
24. Saluzzo S, Gorki AD, Rana BMJ, Martins R, Scanlon S, Starkl P, et al. First-Breath-Induced Type 2 Pathways Shape the Lung Immune Environment. *Cell Rep*. 2017;18(8):1893-905.
25. Galic S, Fullerton MD, Schertzer JD, Sikkema S, Marcinko K, Walkley CR, et al. Hematopoietic AMPK beta1 reduces mouse adipose tissue macrophage inflammation and insulin resistance in obesity. *J Clin Invest*. 2011;121(12):4903-15.
26. Raichur S, Wang ST, Chan PW, Li Y, Ching J, Chaurasia B, et al. CerS2 haploinsufficiency inhibits beta-oxidation and confers susceptibility to diet-induced steatohepatitis and insulin resistance. *Cell Metab*. 2014;20(4):687-95.
27. Ussher JR, Koves TR, Cadete VJ, Zhang L, Jaswal JS, Swyrd SJ, et al. Inhibition of de novo ceramide synthesis reverses diet-induced insulin resistance and enhances whole-body oxygen consumption. *Diabetes*. 2010;59(10):2453-64.
28. Tran TT, and Kahn CR. Transplantation of adipose tissue and stem cells: role in metabolism and disease. *Nature Reviews Endocrinology*. 2010;6(4):195-213.
29. Tran TT, Yamamoto Y, Gesta S, and Kahn CR. Beneficial effects of subcutaneous fat transplantation on metabolism. *Cell Metabolism*. 2008;7(5):410-20.
30. de la Monte SM, and Wands JR. Alzheimer's disease is type 3 diabetes-evidence reviewed. *J Diabetes Sci Technol*. 2008;2(6):1101-13.
31. Gonzalez FJ, Xie C, and Jiang C. The role of hypoxia-inducible factors in metabolic diseases. *Nat Rev Endocrinol*. 2018;15(1):21-32.
32. Strissel KJ, Stancheva Z, Miyoshi H, Perfield JW, 2nd, DeFuria J, Jick Z, et al. Adipocyte death, adipose tissue remodeling, and obesity complications. *Diabetes*. 2007;56(12):2910-8.
33. Oh DY, Morinaga H, Talukdar S, Bae EJ, and Olefsky JM. Increased macrophage migration into adipose tissue in obese mice. *Diabetes*. 2012;61(2):346-54.
34. Fujisaka S, Usui I, Bukhari A, Iikutani M, Oya T, Kanatani Y, et al. Regulatory mechanisms for adipose tissue M1 and M2 macrophages in diet-induced obese mice. *Diabetes*. 2009;58(11):2574-82.

35. Schooneman MG, Vaz FM, Houten SM, and Soeters MR. Acylcarnitines: reflecting or inflicting insulin resistance? *Diabetes*. 2013;62(1):1-8.
36. Turpin SM, Nicholls HT, Willmes DM, Mourier A, Brodesser S, Wunderlich CM, et al. Obesity-induced CerS6-dependent C16:0 ceramide production promotes weight gain and glucose intolerance. *Cell Metab*. 2014;20(4):678-86.
37. Chaurasia B, Tippetts TS, Mayoral Monibas R, Liu J, Li Y, Wang L, et al. Targeting a ceramide double bond improves insulin resistance and hepatic steatosis. *Science*. 2019;365(6451):386-92.
38. Stratford S, Hoehn KL, Liu F, and Summers SA. Regulation of insulin action by ceramide: dual mechanisms linking ceramide accumulation to the inhibition of Akt/protein kinase B. *J Biol Chem*. 2004;279(35):36608-15.
39. Turpin-Nolan SM, Hammerschmidt P, Chen W, Jais A, Timper K, Awazawa M, et al. CerS1-Derived C18:0 Ceramide in Skeletal Muscle Promotes Obesity-Induced Insulin Resistance. *Cell Rep*. 2019;26(1):1-10 e7.
40. Sica A, and Mantovani A. Macrophage plasticity and polarization: in vivo veritas. *J Clin Invest*. 2012;122(3):787-95.
41. Ito A, Suganami T, Yamauchi A, Degawa-Yamauchi M, Tanaka M, Kouyama R, et al. Role of CC chemokine receptor 2 in bone marrow cells in the recruitment of macrophages into obese adipose tissue. *J Biol Chem*. 2008;283(51):35715-23.
42. Holland WL, Miller RA, Wang ZV, Sun K, Barth BM, Bui HH, et al. Receptor-mediated activation of ceramidase activity initiates the pleiotropic actions of adiponectin. *Nat Med*. 2011;17(1):55-63.
43. Takahashi K, Rochford CD, and Neumann H. Clearance of apoptotic neurons without inflammation by microglial triggering receptor expressed on myeloid cells-2. *J Exp Med*. 2005;201(4):647-57.
44. Nawaz A, Aminuddin A, Kado T, Takikawa A, Yamamoto S, Tsuneyama K, et al. CD206(+) M2-like macrophages regulate systemic glucose metabolism by inhibiting proliferation of adipocyte progenitors. *Nat Commun*. 2017;8(1):286.
45. Xia JY, Holland WL, Kusminski CM, Sun K, Sharma AX, Pearson MJ, et al. Targeted Induction of Ceramide Degradation Leads to Improved Systemic Metabolism and Reduced Hepatic Steatosis. *Cell Metab*. 2015;22(2):266-78.
46. Chaurasia B, Kaddai VA, Lancaster GI, Henstridge DC, Sriram S, Galam DL, et al. Adipocyte Ceramides Regulate Subcutaneous Adipose Browning, Inflammation, and Metabolism. *Cell Metab*. 2016;24(6):820-34.
47. Verloes A, Maquet P, Sadzot B, Vivario M, Thiry A, and Franck G. Nasu-Hakola syndrome: polycystic lipomembranous osteodysplasia with sclerosing leucoencephalopathy and presenile dementia. *J Med Genet*. 1997;34(9):753-7.
48. Yokoi S, Suzuki K, Amano N, and Yagishita S. Fatty acid analysis of galactolipids and ganglioside in the brains of four cases of Nasu-Hakola disease. *Jpn J Psychiatry Neurol*. 1989;43(4):695-701.

Author Contributions

OS designed, performed and analyzed data for the majority of the experiments. JB, AK, AH, KL, SS, BB, AV, ADG, JL, DS, GS, MB helped with experiments. RM analyzed adipocyte cell size and performed experiments. AJ and HE performed and analyzed human data, helped with metabolic cages and contributed to project design. BS, MC, JM and GSF analyzed lipidomics data. IM analyzed liver steatosis. KT: mouse husbandry/veterinary. OS and SK conceived the project, OS designed the overall research plan and with SK wrote the manuscript.

Acknowledgements

The authors thank the staff of the animal facility at the Medical University of Vienna. This work was funded by the Austrian Science Fund (FWF P25801 and FWF P31568 to OS) and the special research programs (SFB) Immunothrombosis of the Austrian Science Fund (F5410-B21 to SK). Dr. Omar Sharif and Prof Sylvia Knapp are guarantors of this work and, as such, had full access to all the data in the study and takes responsibility for the integrity of the data and the accuracy of the data analysis.

Declaration of Interests

The authors have declared that no conflict of interest exists.

Figure Legends

Figure 1. Conserved visceral adipose upregulation of TREM2 in obesity. (A) *Trem2* expression in organs post 13 weeks HFD. (B) *Trem2* expression in visceral and subcutaneous adipose depots post 13 weeks HFD. (C) *Trem2* expression in adipose tissue macrophages (ATM) and mature adipocytes (MA). (D) Immunohistochemistry of eWAT depicting TREM2 post 13 weeks HFD. (E) *Trem2* expression in human visceral adipose biopsies obtained from obese insulin-sensitive (ObIS) and obese insulin resistant (ObIR) individuals. Graph bar results are mean \pm SEM, n = 4 per diet. Statistical analysis was performed with Mann Whitney t-test (A-B) or two-way ANOVA followed by Bonferroni post-test (E). * P < 0.05, ** P < 0.01, **** P < 0.0001.

Figure 2. TREM2 deficiency aggravates obesity induced insulin resistance. (A) Insulin tolerance test of WT and *Trem2*^{-/-} mice, 13 weeks post HFD, n = 8 per genotype. (B) Area under the curve (AUC) of (A). (C) Oral glucose test of WT and *Trem2*^{-/-} mice 13 weeks post HFD, n = 8 per genotype. (D) Adipose weights 13 weeks post HFD of animals in (C) RP represents retroperitoneal, eWAT: epididymal, VAT: visceral, SAT: subcutaneous, white adipose tissue depots. (E) Mouse weights 13 weeks post HFD of animals in (C/D). (F-H) Energy expenditure and activity of control and *Trem2*^{-/-} mice 13 weeks post HFD, n = 4 per genotype. Data represent mean \pm SEM and are for (A-E) pooled data from 2 independent experiments. Statistical analysis was performed with two-way ANOVA followed by Bonferroni post-test (A, C), Students t-test (B, D) or one-way ANOVA followed by Tukey post-test (G). * P < 0.05, ** P < 0.01.

Figure 3. Elevated adipose hypertrophy of obese TREM2 deficient animals is associated with ATM remodeling. (A) Representative H&E staining of epididymal white adipose (eWAT) of WT and *Trem2*^{-/-} mice 13 weeks post HFD, n = 8 mice per genotype. (B) Quantification of adipocyte cell size of WT and *Trem2*^{-/-} mice 13 weeks post HFD (n = 8 mice per genotype and data corresponds to size quantification of 3492 WT and 2103 *Trem2*^{-/-} adipocytes). (C) Absolute macrophage content (defined as viable, CD45⁺F4/80⁺CD11b⁺ cells) in eWAT of both genotypes of animals following 13 weeks feeding under both dietary conditions, n = 4 mice per condition. (D) Percentage of macrophages (defined as viable, CD45⁺F4/80⁺ cells) in eWAT of both genotypes of animals 13 weeks post HFD, n = 4 mice per genotype. (E) Ratio of FBC (viable, CD45⁺F4/80⁺CD11b⁺CD11c⁺CD206⁻ cells) versus FB206 (viable, CD45⁺F4/80⁺CD11b⁺CD206⁺ cells) in eWAT of both genotypes of animals following 13 weeks feeding under both dietary conditions, n = 4 mice per genotype. (F) Percentage within the parent FB population of CD206⁺, CD11c⁺, CD206⁺CD11c⁺ ATMs in both genotypes of obese animals 13 weeks post HFD, n = 4 mice per genotype. (G) Representative flow cytometry plots of (F). Graph bar results are mean ± SEM and are for (A-B) pooled data from 2 independent experiments. Data in (E-G) are representative of 2 independent experiments. Statistical analysis was performed with Students t-test (B, D, F) or one-way ANOVA followed by Tukey post-test (C, E). * P < 0.05, ** P < 0.01, **** P < 0.0001, n.s = not significant.

Figure 4: Metabolic stress is required for the protective effects of TREM2 which are linked to elevated sphingolipids levels. (A) Log₂-fold change (FC) in metabolite abundance for *Trem2*^{-/-} over WT mice averaged over both dietary conditions compared with log₂(FC) metabolite levels of HFD over ND averaged over both genetic groups, n = 3 or 4 mice per genotype following 14

weeks of ND or HFD respectively. **(B)** Glucose levels (x-axis) versus relative abundance of selected lipids (y-axis) following 45 and 60 min of insulin challenge. Dots represent mice, colored as indicated in legend. **(C)** Activation of liver AKT signaling 5 min post insulin injection in both genotypes fed a HFD for 13 weeks. **(D)** Scheme for sphingolipid blockage. WT or *Trem2*^{-/-} mice were placed on a HFD for 13 or 26 weeks. Eight weeks post DIO, mice were injected 3 x weekly with saline control or myriocin at a dose of 0.5mg/kg and maintained on a HFD. **(E)** Log₂-fold change (FC) in average abundance of short, long and ultra-long chained ceramides for both genotypes of myriocin treated animals compared saline controls, n = 4 mice per condition post 26 weeks of HFD. **(F)** Insulin tolerance test of both genotypes of mice in the context of sphingolipid blockage, 13 weeks post HFD, n = 8-9 mice per condition. **(G)** Area under the curve (AUC) and mouse weights of data in **(F)**. **(H)** Representative H&E staining of epididymal white adipose (eWAT), 13 weeks post HFD of animals in **(F/G)**, n = 8-9 mice per condition. **(I)** Quantification of adipocyte cell size in **(H)**. Results are mean ± SEM. Statistical analysis was performed with two-way ANOVA followed by Bonferroni post-test **(F)** or one-way ANOVA followed by Tukey post-test **(G, I)**. * P < 0.05, ** P < 0.01, *** P < 0.001, **** P < 0.0001, n.s. = not significant.

Figure 5: Sphingolipid blockage exerts no effects on the ATM compartment of *Trem2*^{-/-} mice

(A) Absolute eWAT macrophage content of both genotypes of animals (defined as viable, CD45⁺F4/80⁺CD11b⁺ cells) in the context of sphingolipid blockage, 13 weeks post HFD, n = 5 mice per condition. **(B-C)** Percentage within the parent FB population of CD206⁺ and CD11c⁺ ATMs in both genotypes of obese animals, 13 weeks post HFD in the context of sphingolipid blockage, n = 5 mice per condition. **(D)** ATM mediated polarization and inflammation from flow

assisted cell sorted viable, CD45⁺CD3⁻F4/80⁺CD11b⁺ cells of both genotypes of animals in the context of sphingolipid blockage, 13 weeks post HFD, n = 3-5 mice per condition. Data are depicted as fold-change to WT saline animals. **(E)** Percentage of macrophages (defined as viable, CD45⁺F4/80⁺CD11b⁺ cells) in eWAT of both genotypes of animals in the context of sphingolipid blockage, 13 weeks post HFD, n = 3-5 mice per condition. **(F)** Percentage of BODIPY⁺ macrophages (defined as viable, BODIPY⁺CD45⁺F4/80⁺CD11b⁺ cells) in eWAT of both genotypes of animals in the context of sphingolipid blockage, 13 weeks post HFD, n = 3-5 mice per condition. Results are mean ± SEM. Statistical analysis was performed with one-way ANOVA followed by Tukey post-test **(A-C, E-F)**. * P < 0.05, **** P < 0.0001.

Figure 6. TREM2 exerts protective effects in sphingolipid mediated secondary liver steatosis associated with specific defects in visceral ATM content. **(A)** Insulin tolerance test 26 weeks post HFD, n = 4 per genotype. **(B)** Liver size 26 weeks post HFD, n = 4 per genotype. **(C)** Liver steatosis 26 weeks post HFD, n = 4 per genotype. **(D)** Ratio of FBC (viable, CD45⁺F4/80⁺CD11b⁺CD11c⁺ cells) versus FB206 (viable, CD45⁺ F4/80⁺ CD11b⁺CD206⁺ cells) in eWAT of both genotypes of animals 26 weeks post HFD, n = 4 mice per genotype. **(E)** Percentage of macrophages (viable, CD45⁺Ly6G⁻F4/80⁺) in eWAT 26 weeks post HFD, n = 4 per genotype. **(F)** Representative flow cytometry plots of **(E)**. **(G)** % WBC evaluated using flow cytometry 26 weeks post HFD, n = 4 per genotype. **(H)** MCP-1 levels and protein content in adipocyte conditioned media (ACM) derived from WT and *Trem-2*^{-/-} mice following 26 weeks HFD, n = 5 mice per genotype. **(I)** Migration levels of bone marrow (BM) macrophages induced by ACM in **(H)**, n = 4 per condition. **(J)** Representative liver morphology and H&E staining, 26 weeks post HFD in the context of sphingolipid blockage, n = 4-5 mice per genotype. **(K)** Liver

steatosis 26 weeks post HFD in the context of sphingolipid blockage, $n = 4-5$ mice per genotype. Results are mean \pm SEM. Data in **(A-F, H-I)** are representative of 2 independent experiments. Statistical analysis was performed with two-way ANOVA followed by Bonferroni post-test **(A)**, Students t-test **(C-E, H)** or one-way ANOVA followed by Tukey post-test **(I and K)**. * $P < 0.05$, ** $P < 0.01$, *** $P < 0.001$, **** $P < 0.0001$, n.s. = not significant.

Figure 7. Uncoupling of hematopoietic expressed TREM2's effects on adipose hypertrophy and metabolic health. **(A)** Scheme for bone marrow transplantation studies. WT or *Trem2*^{-/-} mice were lethally irradiated and transplanted to either WT or *Trem2*^{-/-} bone marrow to generate 4 groups of mice; WT (WT>WT), *Trem2*^{-/-} (*Trem2*^{-/-}>*Trem2*^{-/-}) or chimeric mice - WT mice with *Trem2*^{-/-} bone marrow (*Trem2*^{-/-}>WT) and *Trem2*^{-/-} transplanted with WT bone marrow (WT>*Trem2*^{-/-}). Post-transplant mice were maintained on a normal chow diet (ND) for 6 weeks, following which DIO was instigated. **(B)** Insulin tolerance test 13 weeks post HFD. **(C)** AUC of data in **(B)**. **(D)** Oral glucose tolerance test 13 weeks post HFD. **(E)** AUC of data in **(D)**. **(F)** Representative H&E, TREM-2 and F4/80 staining of epididymal white adipose of bone marrow transplanted mice 26 weeks post HFD. **(G)** Quantification of adipocyte cell size in H&E staining from **(F)**. Data corresponds to size quantification of 3868, 3147, 3198, and 4412 adipocytes in WT>WT, *Trem2*^{-/-}>WT, *Trem2*^{-/-}> *Trem2*^{-/-} and WT> *Trem2*^{-/-} mice respectively. Results are mean \pm SEM and are pooled data from 2 independent experiments, $n = 10-13$ mice per genotype. Statistical analysis was performed with two-way ANOVA followed by Bonferroni post-test **(B and D)** or one-way ANOVA followed by Tukey post-test **(C, E, G)**. * $P < 0.05$, ** $P < 0.01$, *** $P < 0.01$, **** $P < 0.0001$.

Figure 8. Effects of TREM2 on hepatic steatosis are linked to non-hematopoietic tissue and elevated adipose ceramide levels.

(A) Liver aspects and stainings of representative liver sections (H&E, oil Red O, Ceramide) and representative whole-mount of epididymal white adipose of bone marrow transplanted mice 26 weeks post HFD. (B) Liver steatosis in groups of bone marrow transplanted mice 26 weeks post HFD. (C) Serum levels of ALT 26 weeks post HFD. (D) Average abundance of short, long and ultra-long ceramide species in epididymal white adipose of bone marrow transplanted mice 26 weeks post HFD. Individual ceramide abundances scaled between 0 (minimum) and 1 (maximum), n = 4 mice per genotype (E) Serum adiponectin levels 26 weeks post HFD. Results in (B, C, E) are mean \pm SEM and are pooled data from 2 independent experiments, n = 10-13 mice per genotype. Statistical analysis was performed with one-way ANOVA followed by Tukey post-test (B, C, E). * P < 0.05, ** P < 0.01, *** P < 0.01, **** P < 0.0001.

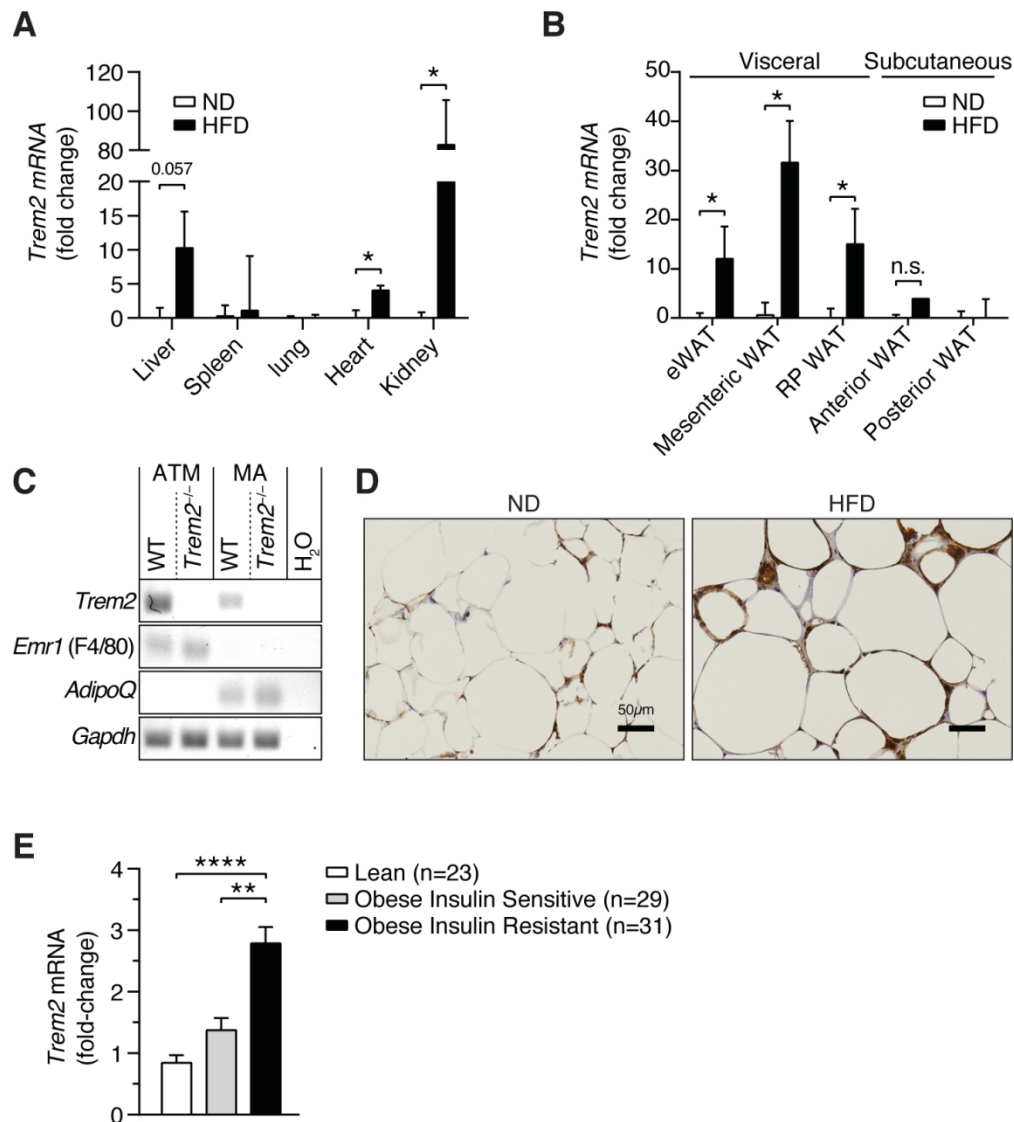


Figure. 1. Conserved visceral adipose upregulation of TREM2 in obesity. (A) Trem2 expression in organs post 13 weeks HFD. (B) Trem2 expression in visceral and subcutaneous adipose depots post 13 weeks HFD. (C) Trem2 expression in adipose tissue macrophages (ATM) and mature adipocytes (MA). (D) Immunohistochemistry of eWAT depicting TREM2 post 13 weeks HFD. (E) Trem2 expression in human visceral adipose biopsies obtained from obese insulin-sensitive (ObIS) and obese insulin resistant (ObIR) individuals. Graph bar results are mean \pm SEM, n = 4 per diet. Statistical analysis was performed with Mann Whitney t-test (A-B) or two-way ANOVA followed by Bonferroni post-test (E). * P < 0.05, ** P < 0.01, **** P < 0.0001.

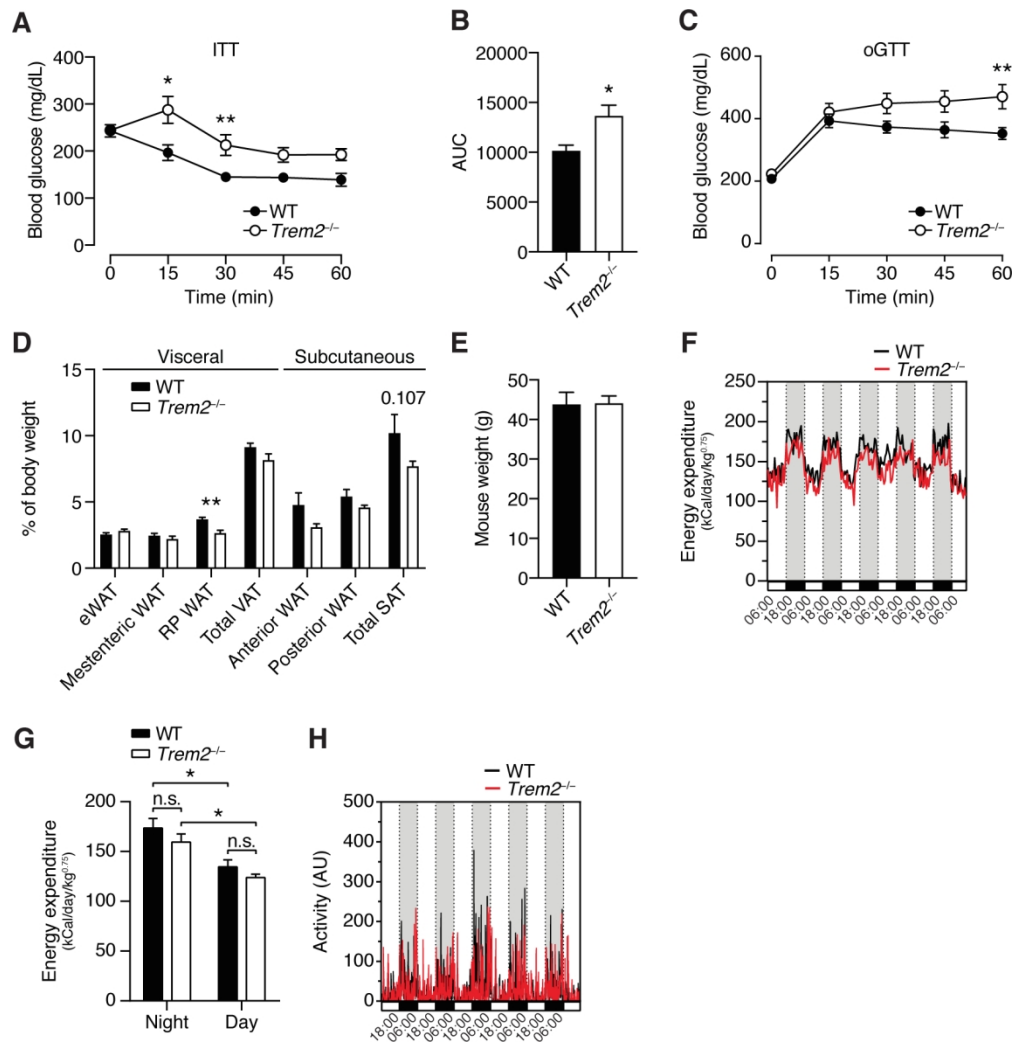


Figure 2. TREM2 deficiency aggravates obesity induced insulin resistance. (A) Insulin tolerance test of WT and Trem2^{-/-} mice, 13 weeks post HFD, n = 8 per genotype. (B) Area under the curve (AUC) of (A). (C) Oral glucose test of WT and Trem2^{-/-} mice 13 weeks post HFD, n = 8 per genotype. (D) Adipose weights 13 weeks post HFD of animals in (C) RP represents retroperitoneal, eWAT: epididymal, VAT: visceral, SAT: subcutaneous, white adipose tissue depots. (E) Mouse weights 13 weeks post HFD of animals in (C/D). (F-H) Energy expenditure and activity of control and Trem2^{-/-} mice 13 weeks post HFD, n = 4 per genotype. Data represent mean \pm SEM and are for (A-E) pooled data from 2 independent experiments. Statistical analysis was performed with two-way ANOVA followed by Bonferroni post-test (A, C), Students t-test (B, D) or one-way ANOVA followed by Tukey post-test (G). * P < 0.05, ** P < 0.01.

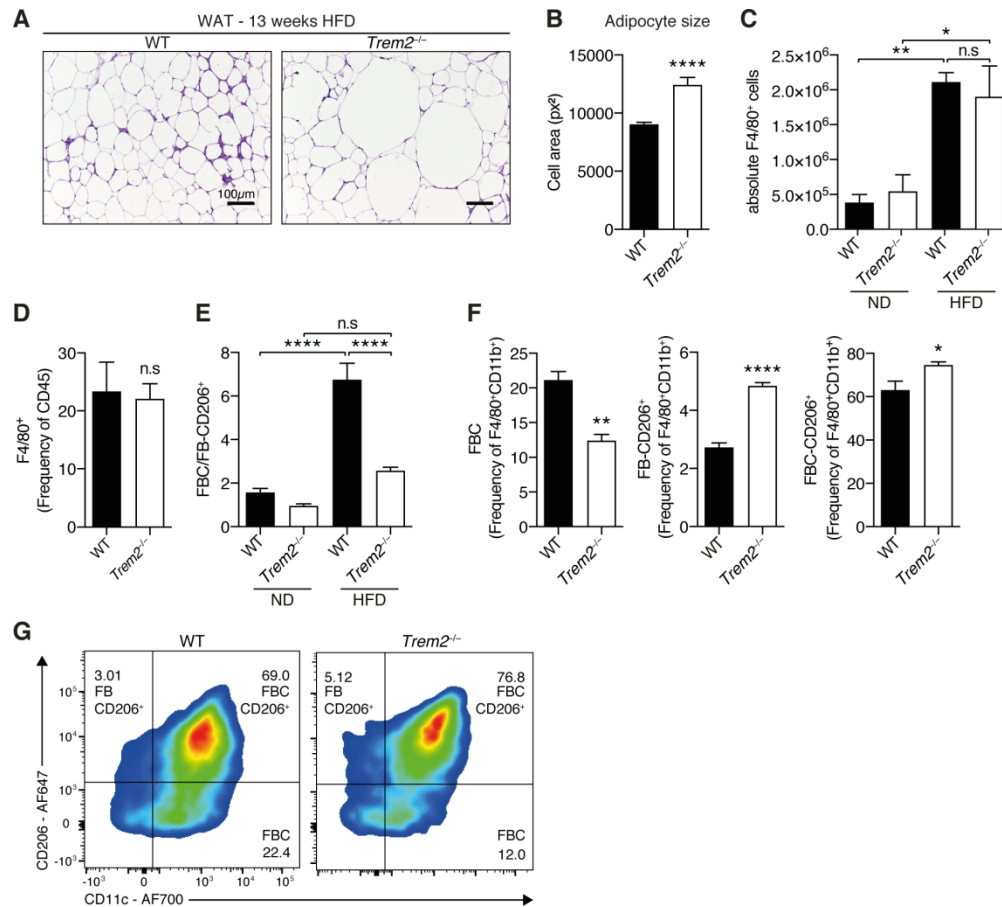


Figure 3. Elevated adipose hypertrophy of obese TREM2 deficient animals is associated with ATM remodeling. (A) Representative H&E staining of epididymal white adipose (eWAT) of WT and Trem2^{-/-} mice 13 weeks post HFD, n = 8 mice per genotype. (B) Quantification of adipocyte cell size of WT and Trem2^{-/-} mice 13 weeks post HFD (n = 8 mice per genotype and data corresponds to size quantification of 3492 WT and 2103 Trem2^{-/-} adipocytes). (C) Absolute macrophage content (defined as viable, CD45⁺F4/80⁺CD11b⁺ cells) in eWAT of both genotypes of animals following 13 weeks feeding under both dietary conditions, n = 4 mice per condition. (D) Percentage of macrophages (defined as viable, CD45⁺F4/80⁺ cells) in eWAT of both genotypes of animals 13 weeks post HFD, n = 4 mice per genotype. (E) Ratio of FBC (viable, CD45⁺F4/80⁺CD11b⁺CD11c⁺CD206⁻ cells) versus FB206 (viable, CD45⁺F4/80⁺CD11b⁺CD206⁺ cells) in eWAT of both genotypes of animals following 13 weeks feeding under both dietary conditions, n = 4 mice per genotype. (F) Percentage within the parent FB population of CD206⁺, CD11c⁺, CD206⁺CD11c⁺ ATMs in both genotypes of obese animals 13 weeks post HFD, n = 4 mice per genotype. (G) Representative flow cytometry plots of (F). Graph bar results are mean ± SEM and are for (A-B) pooled data from 2 independent experiments. Data in (E-G) are representative of 2 independent experiments. Statistical analysis was performed with Student's t-test (B, D, F) or one-way ANOVA followed by Tukey post-test (C, E). * P < 0.05, ** P < 0.01, **** P < 0.0001, n.s = not significant.

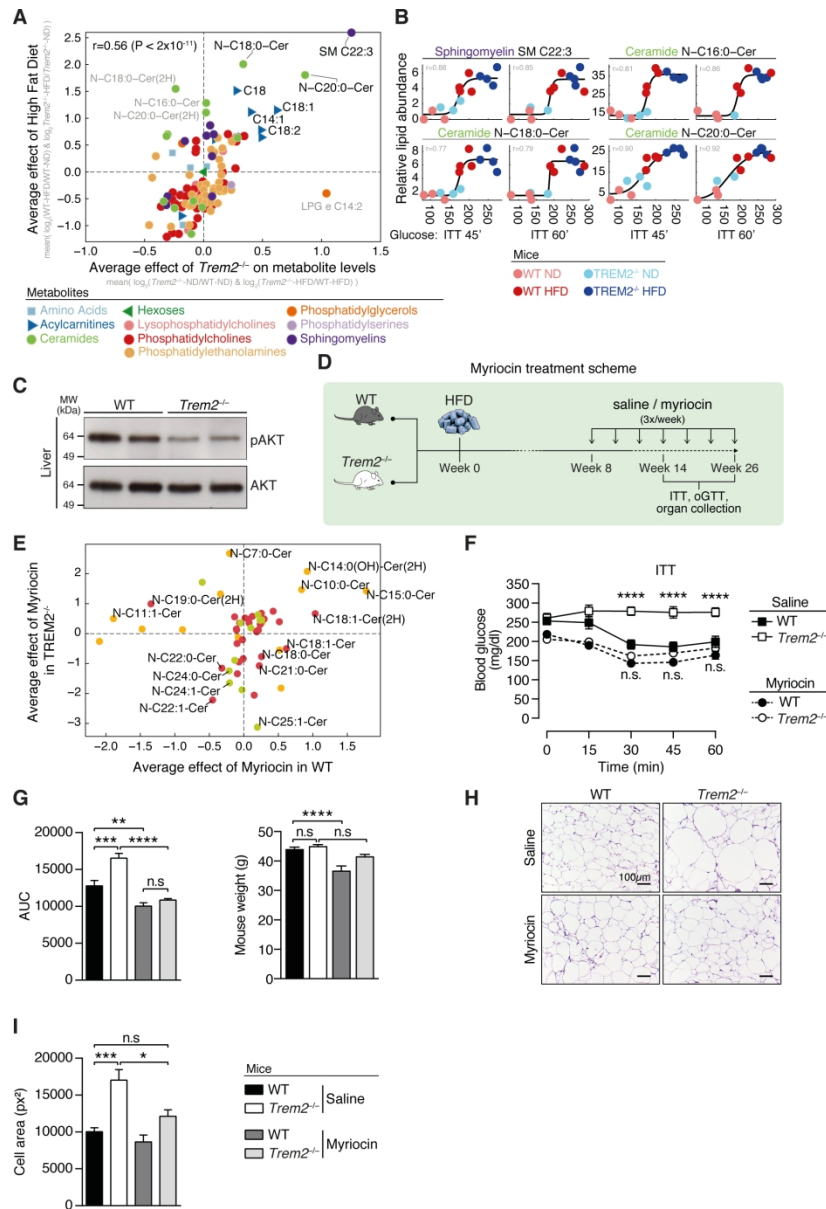


Figure 4: Metabolic stress is required for the protective effects of TREM2 which are linked to elevated sphingolipids levels. (A) Log₂-fold change (FC) in metabolite abundance for *Trem2*^{-/-} over WT mice averaged over both dietary conditions compared with log₂(FC) metabolite levels of HFD over ND averaged over both genetic groups, $n = 3$ or 4 mice per genotype following 14 weeks of ND or HFD respectively. (B) Glucose levels (x-axis) versus relative abundance of selected lipids (y-axis) following 45 and 60 min of insulin challenge. Dots represent mice, colored as indicated in legend. (C) Activation of liver AKT signaling 5 min post insulin injection in both genotypes fed a HFD for 13 weeks. (D) Scheme for sphingolipid blockage. WT or *Trem2*^{-/-} mice were placed on a HFD for 13 or 26 weeks. Eight weeks post DIO, mice were injected 3 x weekly with saline control or myriocin at a dose of 0.5mg/kg and maintained on a HFD. (E) Log₂-fold change (FC) in average abundance of short, long and ultra-long chained ceramides for both genotypes of myriocin treated animals compared saline controls, $n = 4$ mice per condition post 26 weeks of HFD. (F) Insulin tolerance test of both genotypes of mice in the context of sphingolipid blockage, 13 weeks post HFD, $n = 8-9$ mice per condition. (G) Area under the curve (AUC) and mouse weights of data in (F). (H) Representative H&E staining of epididymal white adipose (eWAT), 13 weeks post HFD of animals in (F/G), n

= 8-9 mice per condition. (I) Quantification of adipocyte cell size in (H). Results are mean \pm SEM. Statistical analysis was performed with two-way ANOVA followed by Bonferroni post-test (F) or one-way ANOVA followed by Tukey post-test (G, I). * $P < 0.05$, ** $P < 0.01$, *** $P < 0.001$, **** $P < 0.0001$, n.s. = not significant.

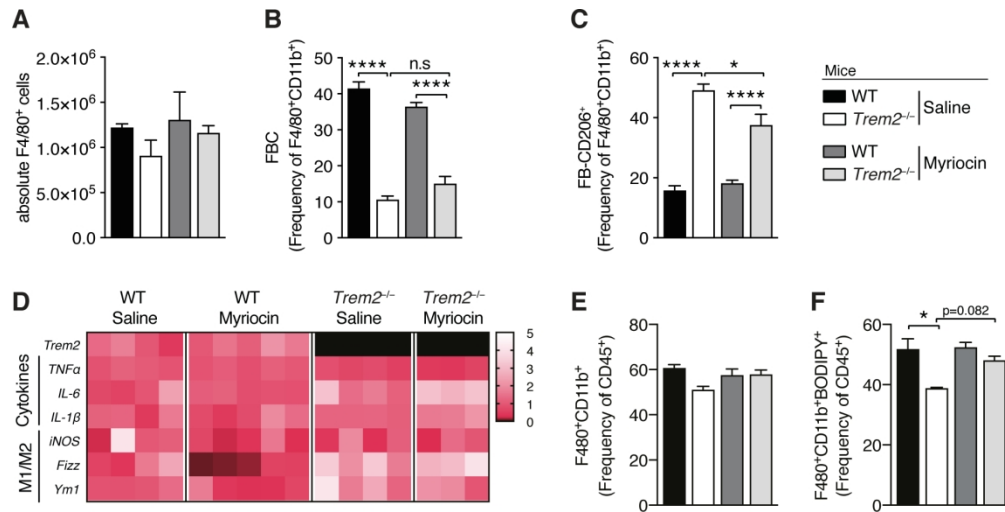


Figure 5: Spingolipid blockage exerts no effects on the ATM compartment of Trem2^{-/-} mice
 (A) Absolute eWAT macrophage content of both genotypes of animals (defined as viable, CD45+F4/80+CD11b+ cells) in the context of sphingolipid blockage, 13 weeks post HFD, n = 5 mice per condition. (B-C) Percentage within the parent FB population of CD206+ and CD11c+ ATMs in both genotypes of obese animals, 13 weeks post HFD in the context of sphingolipid blockage, n = 5 mice per condition. (D) ATM mediated polarization and inflammation from flow assisted cell sorted viable, CD45+CD3-F4/80+CD11b+ cells of both genotypes of animals in the context of sphingolipid blockage, 13 weeks post HFD, n = 3-5 mice per condition. Data are depicted as fold-change to WT saline animals. (E) Percentage of macrophages (defined as viable, CD45+F4/80+CD11b+ cells) in eWAT of both genotypes of animals in the context of sphingolipid blockage, 13 weeks post HFD, n = 3-5 mice per condition. (F) Percentage of BODIPY+ macrophages (defined as viable, BODIPY+CD45+F4/80+CD11b+ cells) in eWAT of both genotypes of animals in the context of sphingolipid blockage, 13 weeks post HFD, n = 3-5 mice per condition. Results are mean ± SEM. Statistical analysis was performed with one-way ANOVA followed by Tukey post-test (A-C, E-F). * P < 0.05, **** P < 0.0001.

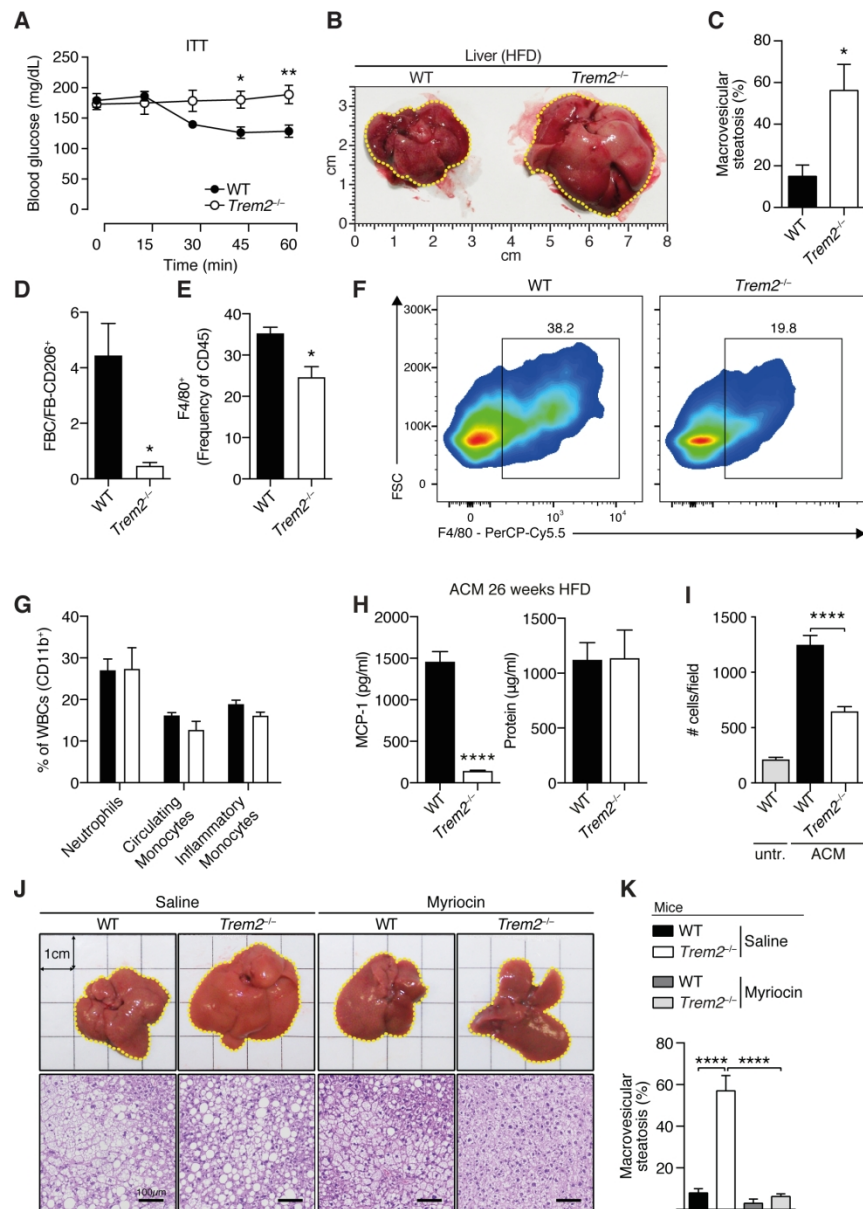


Figure 6. TREM2 exerts protective effects in sphingolipid mediated secondary liver steatosis associated with specific defects in visceral ATM content. (A) Insulin tolerance test 26 weeks post HFD, $n = 4$ per genotype. (B) Liver size 26 weeks post HFD, $n = 4$ per genotype. (C) Liver steatosis 26 weeks post HFD, $n = 4$ per genotype. (D) Ratio of FBC (viable, CD45+F4/80+CD11b+CD11c+ cells) versus FB206 (viable, CD45+F4/80+CD11b+CD206+ cells) in eWAT of both genotypes of animals 26 weeks post HFD, $n = 4$ mice per genotype. (E) Percentage of macrophages (viable, CD45+Ly6G-F4/80+) in eWAT 26 weeks post HFD, $n = 4$ per genotype. (F) Representative flow cytometry plots of (E). (G) % WBCs evaluated using flow cytometry 26 weeks post HFD, $n = 4$ per genotype. (H) MCP-1 levels and protein content in adipocyte conditioned media (ACM) derived from WT and Trem2^{-/-} mice following 26 weeks HFD, $n = 5$ mice per genotype. (I) Migration levels of bone marrow (BM) macrophages induced by ACM in (H), $n = 4$ per condition. (J) Representative liver morphology and H&E staining, 26 weeks post HFD in the context of sphingolipid blockage, $n = 4-5$ mice per genotype. (K) Liver steatosis 26 weeks post HFD in the context of sphingolipid blockage, $n = 4-5$ mice per genotype. Results are mean \pm SEM. Data in (A-F, H-I) are representative of 2 independent experiments. Statistical analysis was performed with two-way ANOVA followed by Bonferroni post-test (A), Students t-test

(C-E, H) or one-way ANOVA followed by Tukey post-test (I and K). * $P < 0.05$, ** $P < 0.01$, *** $P < 0.001$, **** $P < 0.0001$, n.s. = not significant.

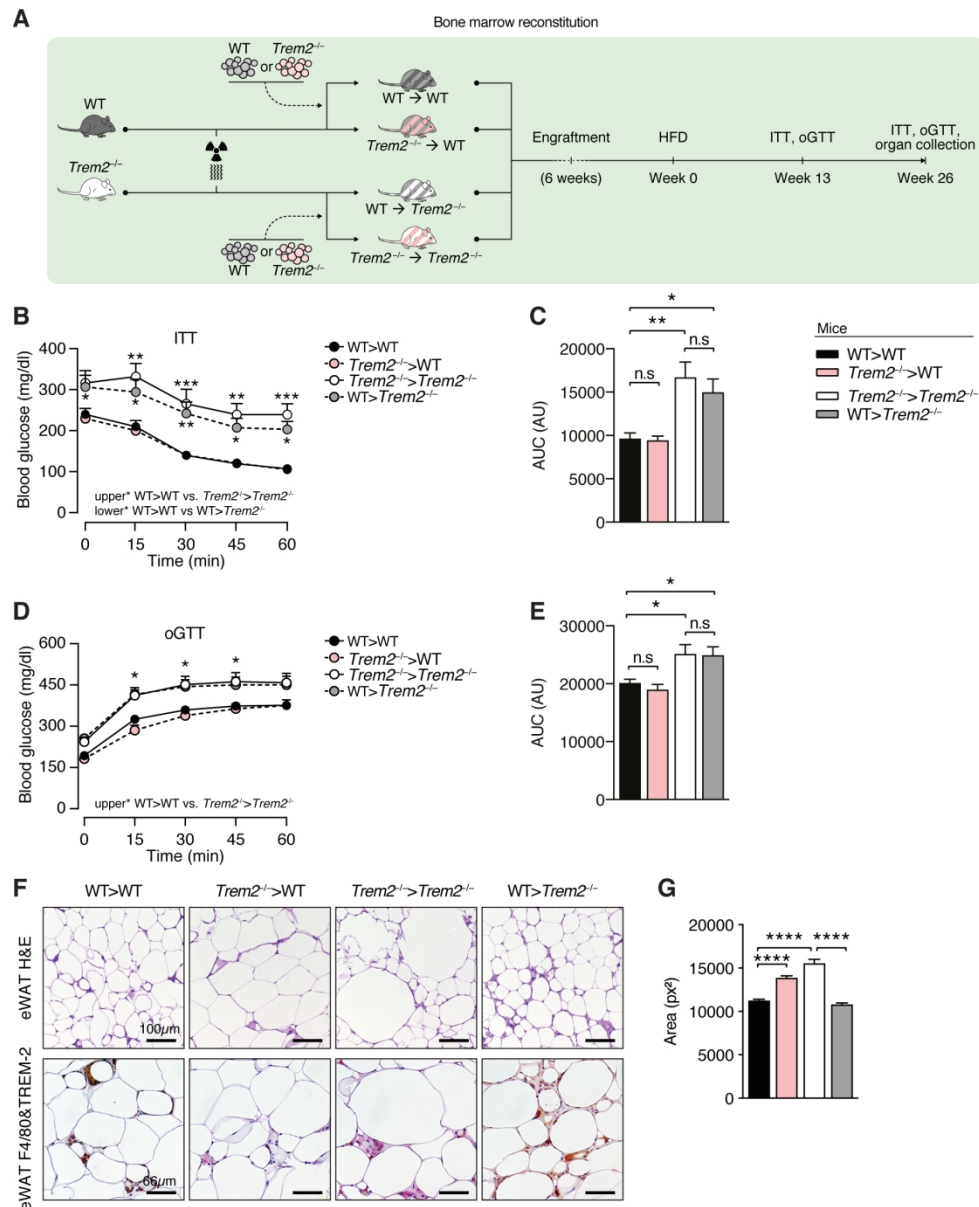


Figure 7. Uncoupling of hematopoietic expressed TREM2's effects on adipose hypertrophy and metabolic health. (A) Scheme for bone marrow transplantation studies. WT or Trem2^{-/-} mice were lethally irradiated and transplanted to either WT or Trem2^{-/-} bone marrow to generate 4 groups of mice; WT (WT>WT), Trem2^{-/-} (Trem2^{-/-}>Trem2^{-/-}) or chimeric mice - WT mice with Trem2^{-/-} bone marrow (Trem2^{-/-}>WT) and Trem2^{-/-} transplanted with WT bone marrow (WT>Trem2^{-/-}). Post-transplant mice were maintained on a normal chow diet (ND) for 6 weeks, following which DIO was instigated. (B) Insulin tolerance test 13 weeks post HFD. (C) AUC of data in (B). (D) Oral glucose tolerance test 13 weeks post HFD. (E) AUC of data in (D). (F) Representative H&E, TREM-2 and F4/80 staining of epididymal white adipose of bone marrow transplanted mice 26 weeks post HFD. (G) Quantification of adipocyte cell size in H&E staining from (F). Data corresponds to size quantification of 3868, 3147, 3198, and 4412 adipocytes in WT>WT, Trem2^{-/-}>WT, Trem2^{-/-}> Trem2^{-/-} and WT> Trem2^{-/-} mice respectively. Results are mean \pm SEM and are pooled data from 2 independent experiments, n = 10-13 mice per genotype. Statistical analysis was performed with two-way ANOVA followed by Bonferroni post-test (B and D) or one-way ANOVA followed by Tukey post-test (C, E, G). * P < 0.05, ** P < 0.01, *** P < 0.01, **** P < 0.0001.

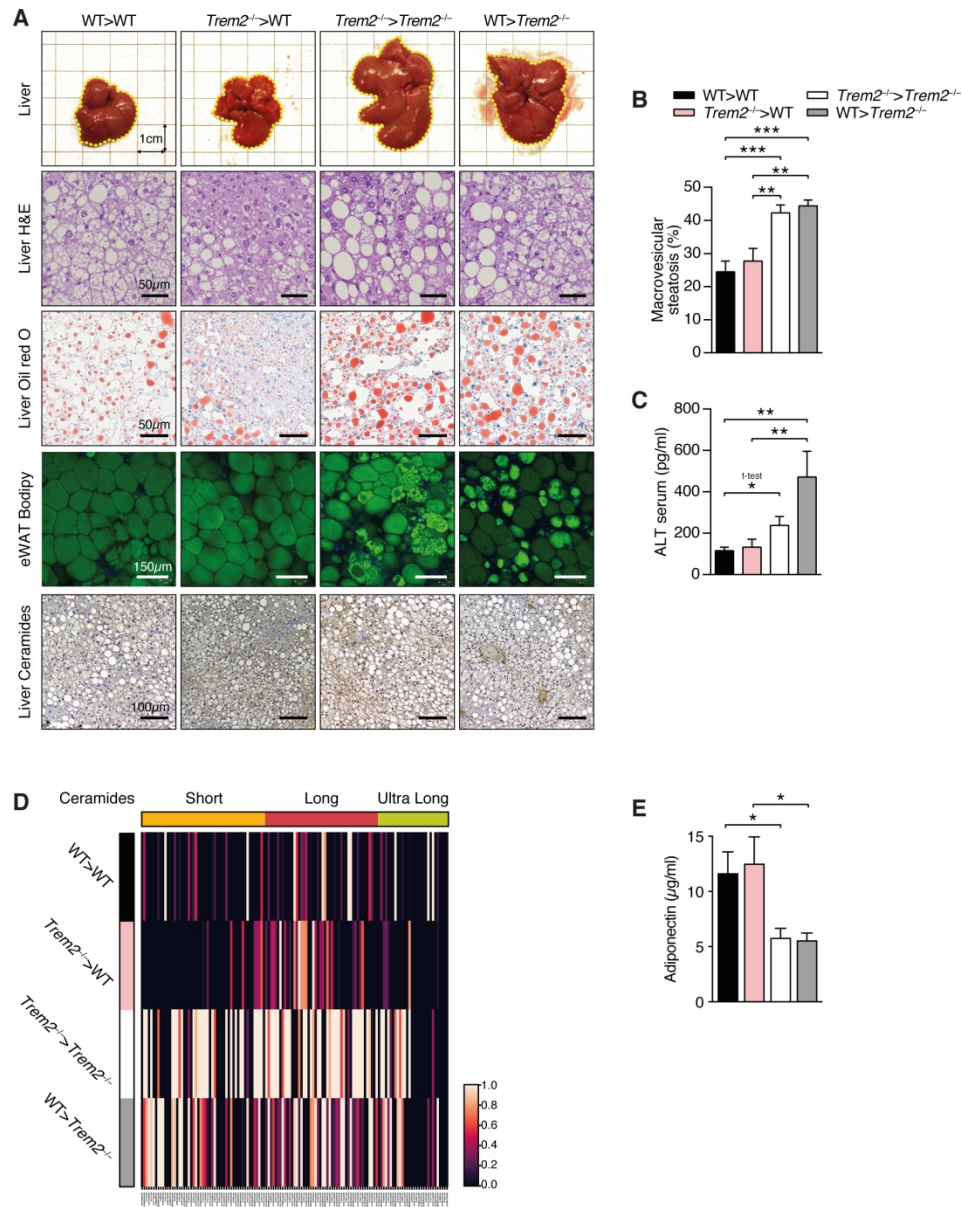


Figure 8. Effects of TREM2 on hepatic steatosis are linked to non-hematopoietic tissue and elevated adipose ceramide levels.

(A) Liver aspects and stainings of representative liver sections (H&E, oil Red O, Ceramide) and representative whole-mount of epididymal white adipose of bone marrow transplanted mice 26 weeks post HFD. (B) Liver steatosis in groups of bone marrow transplanted mice 26 weeks post HFD. (C) Serum levels of ALT 26 weeks post HFD. (D) Average abundance of short, long and ultra-long ceramide species in epididymal white adipose of bone marrow transplanted mice 26 weeks post HFD. Individual ceramide abundances scaled between 0 (minimum) and 1 (maximum), $n = 4$ mice per genotype (E) Serum adiponectin levels 26 weeks post HFD. Results in (B, C, E) are mean \pm SEM and are pooled data from 2 independent experiments, $n = 10-13$ mice per genotype. Statistical analysis was performed with one-way ANOVA followed by Tukey post-test (B, C, E). * $P < 0.05$, ** $P < 0.01$, *** $P < 0.01$, **** $P < 0.0001$.

Beneficial metabolic effects of TREM2 in obesity are uncoupled from its expression on macrophages

Omar Sharif^{1,2,3,4*}, Julia Stefanie Brunner^{1,2,3,4,12}, Ana Korosec^{1,2,13}, Rui Martins^{1,2,14}, Alexander Jais^{5,15}, Berend Snijder^{2,16}, Andrea Vogel^{3,4}, Michael Caldera⁶, Anastasiya Hladik^{1,2}, Karin Lakovits^{1,2}, Simona Saluzzo^{1,2,17}, Benedikta Boehm^{1,2}, Anna-Dorothea Gorki^{1,2}, Ildiko Mesteri⁷, Josefine Lindroos-Christensen^{5,18}, Katharina Tillmann⁸, Dagmar Stoiber^{9,10}, Jörg Menche^{2,6,11}, Gernot Schabbauer^{3,4}, Martin Bilban⁵, Giulio Superti-Furga^{2,9}, Harald Esterbauer⁵ and Sylvia Knapp^{1,2*}

¹Department of Medicine I, Laboratory of Infection Biology, Medical University of Vienna, Vienna, Austria. ²Research Center for Molecular Medicine of the Austrian Academy of Sciences, 1090 Vienna, Austria. ³Institute for Vascular Biology, Centre for Physiology and Pharmacology, Medical University Vienna, Vienna, Austria. ⁴Christian Doppler Laboratory for Arginine Metabolism in Rheumatoid Arthritis and Multiple Sclerosis, Vienna, Austria. ⁵Department of Laboratory Medicine, Medical University of Vienna, Vienna, Austria. ⁶Department of Structural and Computational Biology, Max Perutz Labs, University of Vienna, Campus Vienna Biocenter 5, A-1030 Vienna, Austria. ⁷Institute of Pathology, Überlingen, Germany. ⁸Center of Biomedical Research, Medical University of Vienna, Vienna, Austria. ⁹Institute of Pharmacology, Center of Physiology and Pharmacology, Medical University of Vienna, Vienna, Austria. ¹⁰Department of Pharmacology, Physiology and Microbiology, Division Pharmacology, Karl Landsteiner University of Health Sciences, Krems, Austria. ¹¹Faculty of Mathematics, University of Vienna, Oskar-Morgenstern-Platz 1, A-1090 Vienna, Austria. ¹²Present address: Cell Biology Program, Sloan Kettering Institute, Memorial Sloan Kettering Cancer Center, New York, NY, USA.

¹³Present address: Skin, Endothelium Research Division, Department of Dermatology, Medical University of Vienna, Vienna, Austria. ¹⁴Present address: Instituto Gulbenkian de Ciência, Oeiras, Portugal. ¹⁵Present address: Helmholtz Institute for Metabolic, Obesity and Vascular Research (HI-MAG), Leipzig, Germany. ¹⁶Present address: Department of Biology, Institute of Molecular Systems Biology, ETH Zurich, Zurich, Switzerland. ¹⁷Present address: Department of Dermatology, Medical University of Vienna, Vienna Austria. ¹⁸Present address: Novo Nordisk, Søborg, Denmark.

***Correspondence:**

Omar Sharif: Omar.Sharif@meduniwien.ac.at, Tel: +43-1-40160-31108

Sylvia Knapp: Sylvia.Knapp@meduniwien.ac.at, Tel: +43-1-40400-5139

Supplemental Material

In vivo Insulin Signaling

Mice were fasted for 2 hr, anesthetized and injected with insulin (0.75 U/kg). Livers were removed 5 min post injection and flash frozen in liquid nitrogen prior to tissue homogenization.

Indirect Calorimetry

Body-weight-matched mice were placed for 72 hr in individual metabolic cages with free access to food and water connected to an open-circuit, indirect calorimetry system combined with the determination of spontaneous activity by beam breaking (Oxylet, Panlab-Bioseb). Room temperature was 21-23°C and light/dark cycles were of 12 hr. The animals were accustomed to the apparatus during the first 24 hr, followed by measurements. Oxygen consumption (VO_2) and carbon dioxide production (VCO_2) were recorded using a computer-assisted data acquisition program (Metabolism 2.2.01, Panlab Harvard Apparatus). The Respiratory Quotient (RQ) ($[RQ] = VCO_2/VO_2$) was measured. Energy expenditure was calculated using the metabolism software and defined as (in kcal/day/kg^{0.75} = $1.44 \times VO_2 \times [3.815 + 1.232 \times RQ]$).

Mouse Laboratory Parameters and ELISAs

Serum alanine transaminase (ALT), Aspartate transaminase (AST), triglycerides, cholesterol and blood cell counts were quantified with tests certified for *in vitro* diagnostics at the Center of Biomedical Research of the Medical University of Vienna. Adiponectin and MCP-1 levels were quantified using commercially available ELISA kits (R&D Systems, # MRP300, DY479).

Tissue Homogenization

Isolated organs were weighed, 4 times the volume of 0.9% NaCl added and homogenized using MagNA Lyser Green Beads and a tissue homogenizer. 50 μ l of the homogenate was removed for RNA isolation and mixed with 300 μ l of TRIzol. The remaining homogenate was mixed one to one with Greenberger lysis buffer (containing 300 mM NaCl, 30 mM Tris, 2 mM MgCl₂, 2 mM CaCl₂, 1% Triton X-100, supplemented with 1:50 Protease Inhibitor Cocktail (Sigma-Aldrich #P8340)), incubated for 20 min at 4°C, centrifuged for 10 min at 3000 rpm and the supernatant containing proteins frozen at -80°C until needed.

Stromal Vascular Fraction (SVF) Isolation

SVF was isolated as previously described (1-3). Epididymal white adipose (eWAT) fat pads or donor eWAT pieces from adipose transplanted mice were removed, cut into small (approximately 2 mm) pieces and washed 2 x with DMEM:F12 media (Gibco, #11320-074) supplemented with 50 μ g/ml gentamycin (PAA Laboratories, #P11-005) by centrifugation for 8 min at 1800 rpm at room temperature. Adipose was digested in 10 ml of freshly prepared collagenase II solution (1 mg/ml in 1.5% sterile BSA, in DMEM:F12/Gentamycin) and the fat allowed to digest in a shaking waterbath at 37°C for 1 hr. Subsequently, the digested adipose-enzyme solution was filtered through a 100 μ m strainer into 20 ml DMEM:F12 media supplemented with 10% FBS, 50 μ g/ml gentamycin (herein referred to as SVF media) and centrifuged at 1800 rpm (8 min, room temperature). Post centrifugation, three phases formed with mature adipocytes floating on top, an intermediate phase and a pellet containing SVF. If the mature adipocytes were used for the preparation of adipocyte conditioned media (ACM), the upper adipocyte layer was transferred into a fresh tube and processed accordingly as described below. The pellet was resuspended in SVF

media, washed twice and resuspended in 1ml of erythrocyte lysis buffer (Qiagen, #79217) for 5 min, after which 12 ml of SVF media was added, cells were centrifuged and the pellet was resuspended in PBS supplemented with 2% FBS for antibody labelling and flow cytometry.

Generation of Adipocyte Conditioned Media

The mature adipocyte fraction from SVF was washed once with serum-free media and twice with 1x PBS. Subsequently, 2 ml of mature adipocytes were incubated with 5 ml RPMI/1% Penstrep in a T-25 flask for 24 hrs. The medium was then passed through a 100 µm strainer, aliquoted and frozen at -20°C until use.

Isolation of ATMs

SVF was isolated from 13 week HFD animals and the BD IMag Cell Separation System was used for isolating ATMs. The positive selection was conducted according to the protocol provided by the manufacturer using biotinylated anti-mouse CD11c antibody (BD Biosciences, #553800) to select for CD11c⁺ ATMs.

Chemotaxis Assays of Bone Marrow Macrophages.

Bone marrow (BM) macrophages were retrieved from the tibia and the femur of mice and differentiated in RPMI 1640 supplemented with 1% pen/strep, 10% FCS and 10% L929-conditioned medium for 7 days as previously described (4). Chemotaxis was assayed using a Transwell Boyden chamber system. Either RPMI or RPMI supplemented with ACM was added to

12 wells of a 24 well plate. Subsequently, Corning Transwell System filters (pore size 8 μm , Sigma-Aldrich, #CLS3422) were inserted and 5×10^5 BM macrophages were added onto each filter and left at 37°C , 5% CO_2 for 6 hrs for migration to occur. Post migration, 500 μl of PBS was added to the 12 empty wells and the filters were transferred to the PBS containing wells for washing. Chemotactic stimuli were removed, filters were placed back into empty wells, PBS removed and 500 μl of formalin (4% (v/v) formaldehyde solution) was added. Filters were fixed in formalin for 15 min, stained with 0.2% crystal violet (Sigma-Aldrich, #C6158) solution (dissolved in 50% methanol) for 30 min and thoroughly washed again with PBS. Before the filters were mounted onto microscope slides, the cells on the upper side of the filters were removed using a cotton stick. Crystal violet fluorescence was imaged in the red channel using an Olympus FSX100 fluorescence microscope (UPLSAPO 10x objective). 3 to 4 random images of each membrane were taken and then loaded into the CellProfiler software (5). Image illumination correction functions were applied to each image and the red channel converted to grayscale images. The image contrast was enhanced using ImageJ. The enhanced images were loaded into the CellProfiler software and the cells were counted using the “IdentifyPrimaryObjects” module setup to use the adaptive two-class Otsu thresholding method with intensity as the parameter to distinguish clumped objects. The values were exported to an Excel spreadsheet and further analyzed using GraphPad Prism.

Adipocyte Cell Size Quantification

Images of murine WAT for automatic measurement of adipocyte size (area and perimeter) were acquired using an Olympus FSX100 all-in-one microscope system at 10X magnification and image analysis was performed using the CellProfiler software (5). Briefly, the images were loaded onto the software and the analysis pipeline was programmed to convert images to grayscale, using the

combined weights of 1 for blue, 1.5 for green and 0.5 for red. Binary thresholds of the resulting grayscale images were obtained using a manual threshold value of 0.91 without smoothing. Adipocytes were identified as primary objects using binary thresholds from the previous step and shape as the argument to distinguish clumped objects with a smoothing filter of 40px and local maxima suppression for values shorter than 45 px. Cells touching the image borders were excluded from the analysis. Adipocyte shape properties were measured using the cells identified on the previous step and the perimeter and area for each cell was saved to a spreadsheet. The average adipocyte area and perimeter per mouse was then calculated and used for statistical analysis.

Whole-Mount Immunofluorescence

Epididymal white adipose fat pads from obese mice were removed from the indicated mice and placed in 1% paraformaldehyde for 10 min at room temperature. The tissues were washed 3 x with PBS/0.3% Tween-20 (PBST) and cut into finger nail sized pieces, following which they were blocked in 5% BSA in PBST for 1 hr and incubated with BODIPY™ 500/510 C₁, C₁₂ (Thermo Fisher Scientific, #D3823) for 30 min. Subsequently, tissues were washed 2 x for 10 min with PBST, counterstained with DAPI and visualized using a Zeiss LSM 700 Laser Scanning Microscope (Zeiss, Jena, Germany).

Isolation of Liver Mononuclear Cells

Liver mononuclear cells were isolated as previously described (6, 7). Mice were sacrificed and the livers were perfused via the portal vein with HBSS, cut into small pieces and digested for 1 hr at 37°C in RPMI containing 0.05% collagenase/dispase (Roche, #10269638001) and 0.01% trypsin

inhibitor (Thermo Fisher Scientific, #17075029). The liver suspension was pressed through a 40 μm cell strainer, centrifuged at 800 g (10 min, 4°C) and the cell pellet was resuspended in 10 ml RPMI. Cell suspensions were overlaid onto 15 ml of 33% (Vol/Vol) Percoll solution (Sigma-Aldrich, #P1644) and centrifuged for 30 min (no brake, RT). The supernatant was removed and erythrocytes were lysed by resuspending the pellet in 2 ml of red blood cell lysis buffer for 4 min, after which 8 ml of RPMI was added. Cell suspensions were spun at 800 g (5-10 min, 4°C), supernatant was removed and the cells were washed twice with 10 ml RPMI. Cells were subsequently resuspended in PBS/2%FBS and total cell numbers per liver were enumerated using a hemocytometer (Turck chamber) before they were stained for flow cytometry.

Generation of apoptotic thymocytes

For the cleaved caspase 3 control, thymocytes were isolated from C57BL/6 mice and cultured at 6×10^6 in RPMI/10% FCS. Apoptosis was induced by the addition of 1 μM dexamethasone for 16h.

Flow Cytometry and ATM Sorting

Isolated SVF or liver mononuclear cells were resuspended in PBS supplemented with 2% FBS and Fc receptors were blocked with a CD16/CD32 antibody (eBioscience, #14-0161-82, used at 1:1000) for 10 min on ice. Thereafter SVF was stained with antibodies to: CD45.2 BV500 (BD Biosciences, #561487, used at 1:200) or CD45.2 PE (BioLegend, #103106, used at 1:500) or CD45.2-BV650 (BioLegend, #109836, used at 1:100), CD45.1 Pacific blue (BioLegend, #110721, used at 1:100), F4/80 PE-Cy7 (eBioscience, #25-4801-82, used at 1:360) or F4/80 PerCP Cy5.5 (eBioscience, #45-4801-82, used at 1:100) or F4/80-FITC (BioLegend, #123108, used at 1:100),

CD11b PerCP Cy5.5 (eBioscience, #45-0112-82 used at 1:100) or CD11b Pacific Blue (Biolegend, #101223, used at 1:500) or CD11b-BV605 (BioLegend, #101237, used at 1:500), CD11b-PB (Invitrogen, #RM2828, used at 1:100), CD11c AF700 (eBioscience, #56-0114-82, used at 1:80) or CD11c FITC (BD Biosciences, #553801, used at 1:500), CD206 AF647 (Biolegend, #141711, used at 1:600), CD3-APC (eBioscience, #17-0032-82, used at 1:160) and Ly6G FITC (Biolegend, #127605, used at 1:10,000) for 30 min at 4°C.

Isolated liver mononuclear cells were stained with antibodies to: CD45.2 BV500 (BD Biosciences, #561487, used at 1:100), B220 PerCP Cy5.5 (eBioscience, #45-0452-82, used at 1:200), CD3 APC (eBioscience, #17-0032-82, used at 1:200), Ly6G FITC (Biolegend, #127605, used at 1:2000), CD11b AF700 (eBioscience, #56-0112-80, used at 1:500), Ly6C BV605 (Biolegend, #128035, used at 1:100), F4/80 PE-Cy7 (eBioscience, #25-4801-82, used at 1:200) for 30 min at 4°C. Both SVF cells and liver mononuclear cells were subsequently centrifuged at 1250 rpm (5 min, 4°C) and stained with Fixable viability dye eF780/APC-Cy7 (Thermo Fisher Scientific, #65-0865-14, used at 1:2000) at room temperature for 15 min and washed twice with PBS/2% FBS to allow exclusion of dead cells. Lipid content was assessed by staining the cells with BODIPY 493/503 (Fisher Scientific #11540326) for 15 to 30 min at 37°C.

Blood was stained by directly adding the following antibodies: CD11b AF700 (eBioscience, #56-0112-82, used at 1:700), Ly6C BV570 (Biolegend, #128029, used at 1:100) and Ly6G PE (Biolegend, #127607, used at 1:1500), CD45.1 APC (Biolegend, #110713, used at 1:100) and CD45.2 PE (Biolegend, #103106, used at 1:100) for 30 min to 50 µl of sample. Cells were lysed by adding 140 µL ADG lysis buffer (Andergrub Bioresearch) for 10 min, after which 3.5 ml H₂O was added for 7 min. Samples were washed twice with PBS/FCS and analyzed by flow cytometry (BD LSR Fortessa).

For cell sorting, stained ATMs were filtered through a 40 μ M cell strainer and sorted as live, CD45⁺CD3⁻CD11b⁺F4/80⁺ on a FACSAria™ II flow cytometer (BD).

Control stainings for all flow cytometry included single stainings and unstained cells, which served as compensation controls to ensure that emission spectra under the different fluorescences had minimal overlap. Cells were acquired with LSR Fortessa (BD Biosciences) or with a CytoFLEX S Flow Cytometer (Beckman Coulter) and data further analyzed with FlowJo software (TreeStar). ATMs were identified as live, CD45⁺CD11b⁺F4/80⁺ cells and were further sub-gated for CD11c and CD206. Liver macrophages were identified as CD45⁺CD3⁻B220⁻Ly6G⁻CD11b⁺Ly6C⁺F4/80⁺ cells. Neutrophils were defined as CD11b⁺F4/80⁻Ly6G⁺, circulating monocytes as CD11b⁺F4/80⁻Ly6C^{lo} and inflammatory monocytes as CD11b⁺F4/80⁻Ly6C^{hi}.

Histology, Immunohistochemistry, Liver Oil Red O and Steatosis Scoring

Organs were fixed in 7.5% formaldehyde, embedded in paraffin, cut in 2 μ M slices and stained using hematoxylin and eosin (H&E). TREM-2 immunohistochemistry on formalin-fixed, paraffin-embedded mouse eWAT sections was conducted using the TSA Biosystem kit (Perkin Elmer #NEL700A001KT). Briefly, sections were de-paraffinised in xylene and rehydrated in graded ethanol followed with blocking of endogenous peroxidase in 3.5% H₂O₂ in PBS for 10 min. Thereafter, sections were subjected to antigen-retrieval using citrate buffer pH 6.0 (Vector laboratories), incubated with TNB blocking reagent for 45 min and then probed with sheep polyclonal mouse anti-TREM-2 biotinylated antibody (R&D Systems, #BAF1729) at a dilution of 1:200, overnight at 4°C. Subsequently slides were washed with TNT buffer and incubated with SA-HRP according to the manufactures instructions (Perkin Elmer, #NEL700A001KT). Binding was visualized using the Vectastain ABC kit (Vector laboratories, #PK-6100) and sections were

lightly counter stained with haematoxylin (Mayer, Merck), dehydrated, coverslipped and subjected to light microscopy.

Ceramide immunohistochemistry was conducted on xylene de-paraffinised sections, rehydrated in graded ethanol followed with blocking of endogenous peroxidase and alkaline phosphatase in 3.5% H₂O₂ in PBS for 10 min, after which the sections were permbealized with 0.1% Triton-X in PBS. Thereafter, citrate buffer pH 6.0 (Vector laboratories) was used for antigen-retrieval and sections were incubated with 5% goat serum for 10 min and probed with ceramide monoclonal antibody which recognizes C16 and C24 ceramide species (Clone MID 15B4, Enzo Life Sciences, #ALX-804-196-T050) at a dilution of 1:500, overnight at 4°C. Subsequently slides were washed with PBS, incubated with Biotin-SP-conjugated AffiniPure Fab Fragment goat anti-mouse IgG (H+L) (Jackson Immuno Research, # 115-067-003) at a dilution 1:500 for 30 min at room temperature. Binding was visualized using the Vectastain ABC kit (Vector laboratories, #PK-6100) and DAB Substrate Kit, Peroxidase (Vector laboratories, # SK-4100). Sections were stained with haematoxylin (Mayer, Merck), dehydrated, coverslipped and subjected to light microscopy.

TREM-2 and F4/80 double immunohistochemistry was performed on xylene de-paraffinised sections, rehydrated in graded ethanol followed with blocking of endogenous peroxidase in 3.5% H₂O₂ and Levamisole (Fa. Vector, # SP-5000-18) in PBS for 10 min. Thereafter, sections were subjected to antigen-retrieval using citrate buffer pH 6.0 (Vector laboratories), incubated with 2.5 % horse serum for 20 min and probed with Rabbit Polyclonal anti-TREM2 Antibody (THP, #PTG-13483-1-AP) at a dilution of 1:200, overnight at 4°C. Subsequently slides were washed with TBST buffer and incubated with ImmPRESS® HRP Horse Anti-Rabbit IgG Polymer (Vector laboratories, # MP-7401) for 30 min at room temperature. Binding was visualized using the DAB Substrate Kit, Peroxidase (Vector laboratories, # SK-4100). Sections were then incubated with 5%

donkey serum for 20 min and then probed with Rabbit monoclonal [SP115] against F4/80 (Abcam, #ab240946) at a dilution 1:100 for 60 min at room temperature. Subsequently slides were washed with TBST and incubated with Rabbit AP Polymer from the DoubleStain IHC Kit (Abcam, #ab183285) for 30 min at RT. Binding was visualized using the Permanent Red chromogen from the same kit. Sections were stained with haematoxylin (Mayer, Merck), dehydrated, coverslipped and subjected to light microscopy.

For liver oil Red O staining, 8 μ M liver cryosections were stained with oil red O (1% w/v isopropanol, diluted 3:2 in PBS) for 15 min at room temperature and counterstained with hematoxylin according to standard procedures. Liver steatosis was scored on H&E sections by an experienced pathologist who was blinded for the experimental groups. Macrovesicular steatosis and microvesicular steatosis were both separately scored and defined by whether the vacuoles displaced the nucleus to the side by a single fat globule (macrovesicular) or not due to vast numbers of small fat vesicles (microvesicular) and graded from 0-100%.

Western blotting

Liver tissue protein content was determined using the Peirce Protein Assay Kit (Thermo Scientific, #23225). 20 μ g of proteins were resolved by SDS-PAGE and transferred to PVDF membranes (Biorad). Membranes were blocked with 5% BSA in PBS containing 0.05% Tween-20 (PBS-T) and incubated with primary antibodies at 4°C overnight at a concentration of 1:1000. The following antibodies were used: Akt Pan (Cell Signaling, #4691), Phospho-Akt Ser473 (Cell Signaling, #4060), Vincullin (Cell Signaling, #4650), Caspase 3 (Cell Signaling, #9662). Subsequently, membranes were washed 3 times for 10 min with PBST before incubation with anti-rabbit IgG (Cell Signaling, #7074, used at 1:1000 in 5% BSA/PBST). Thereafter, membranes were washed

again 3x 10 min with PBST and the desired protein was detected using enhanced chemiluminescence.

Quantitative Real Time PCR (qRT-PCR)

qRT-PCR was performed as described (8). In brief, total RNA was extracted from respective tissues and cells using TRIzol according to the manufacturer's instructions (Ambion, #15596-018). For RNA purification and cDNA synthesis, equal amounts of RNA (up to 1 µg) were resuspended in 13 µl H₂O and 1.5 µl 10x buffer plus 0.5 µl DNase I taken from the PerfeCta Dnase I Kit (Quanta Biosciences, #95150-01K) for DNA digestion. Samples were incubated at 37°C for 30 min before 1.5 µl Stop solution was added and incubated thereafter at 65°C for another 10 min. Reverse transcription into cDNA was conducted using the iScript cDNA Synthesis Kit according to the manufacturer's instructions (Bio-Rad, #170-8891). qRT-PCR was performed using the iTaq SYBR Green Supermix with ROX according to the supplier (Bio-Rad, #72-5853) or the Luna Universal qPCR Master Mix (New England Biolabs #M3003E). PCR was performed with the StepOnePlus™ Real-Time PCR System (Applied Biosystems). Post amplification melting curve analysis was performed to check for unspecific products and primer-only controls were included to ensure the absence of primer dimers as well as H₂O only controls to check for contamination by genomic DNA. For normalization threshold cycles (Ct-values) were normalized to the housekeepers, Hypoxanthine Guanine Phosphoribosyltransferase (*Hprt*) or Glyceraldehyde 3-phosphate dehydrogenase (*Gapdh*) within each sample to obtain sample-specific ΔC_t values ($= C_{t_{\text{gene of interest}}} - C_{t_{\text{housekeeper}}}$). $2^{-\Delta\Delta C_t}$ values were calculated to obtain fold expression levels, where $\Delta\Delta C_t = (\Delta C_{t_{\text{treatment}}} - \Delta C_{t_{\text{control}}})$. Primer sequences are indicated in Supplementary Table 1.

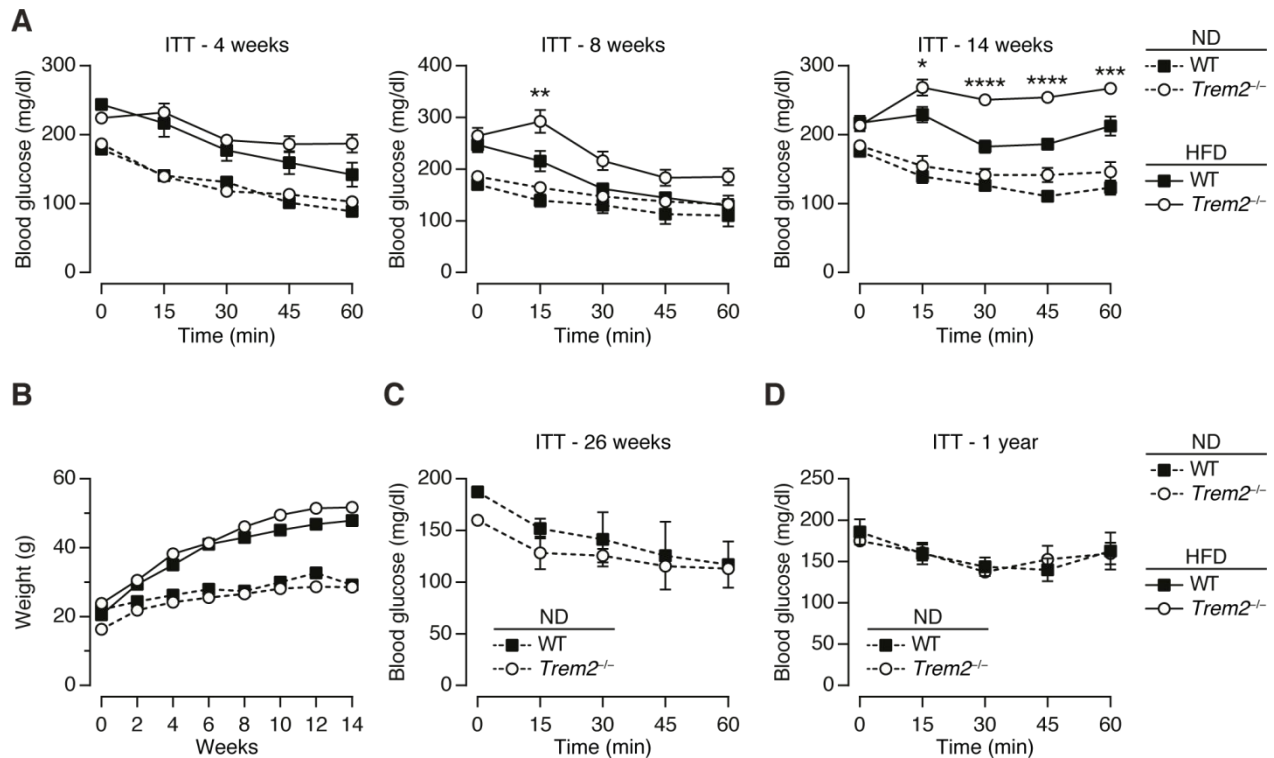
Targeted Metabolomics

Lipidomics was conducted on 20 μ l of serum samples or 50-100mg of homogenized adipose tissue from the indicated mice using a targeted metabolomics approach with BIOCRATES Life Sciences AG (Innsbruck, Austria) as previously described (9, 10). 429 metabolites including 14 amino-acids, 28 hexoses, 40 acylcarnitines, 198 glycerophospholipids (lysophosphatidylcholines (lysoPC), phosphatidylcholines (PC), phosphatidylethanolamines (PE), phosphatidylglycerols (PG), and phosphatidylserines (PS)) and 149 sphingolipids (ceramides (Cer) and sphingomyelins (SM)) were measured. Metabolites were quantified using the in-house validated Partial Lipid Assay and the AbsoluteIDQ® p150 Assay (BIOCRATES Life Sciences AG, Innsbruck, Austria) using tandem mass spectrometry on an AB SCIEX triple-quadrupole mass spectrometer operating in positive and negative MRM mode with analysis performed using the MetIDQ software (BIOCRATES Life Sciences AG, Innsbruck, Austria). In a second set of lipidomics samples employing myrocin treatment or adipose tissue samples, metabolites were only quantified using the in-house validated Partial Lipid Assay and for tissue samples resultant lipid pmol were normalized to adipose weight.

The lipidomics were normalized based on the sum of concentrations for all lipid species measured in a single biological replicate. Values were subsequently averaged over biological replicates for HFD conditions (4 per genotype) and \log_2 transformed against the corresponding average concentrations measured in ND mice (3 per genotype). Significance of pairwise comparisons was calculated using a non-paired two-tailed two-sample *t*-test. Correlations between relative lipid abundance and functional readouts were calculated as Pearson's linear correlation coefficients. For display purposes adjusted Hill-curves were fit to selected relations between relative lipid abundance and functional readouts.

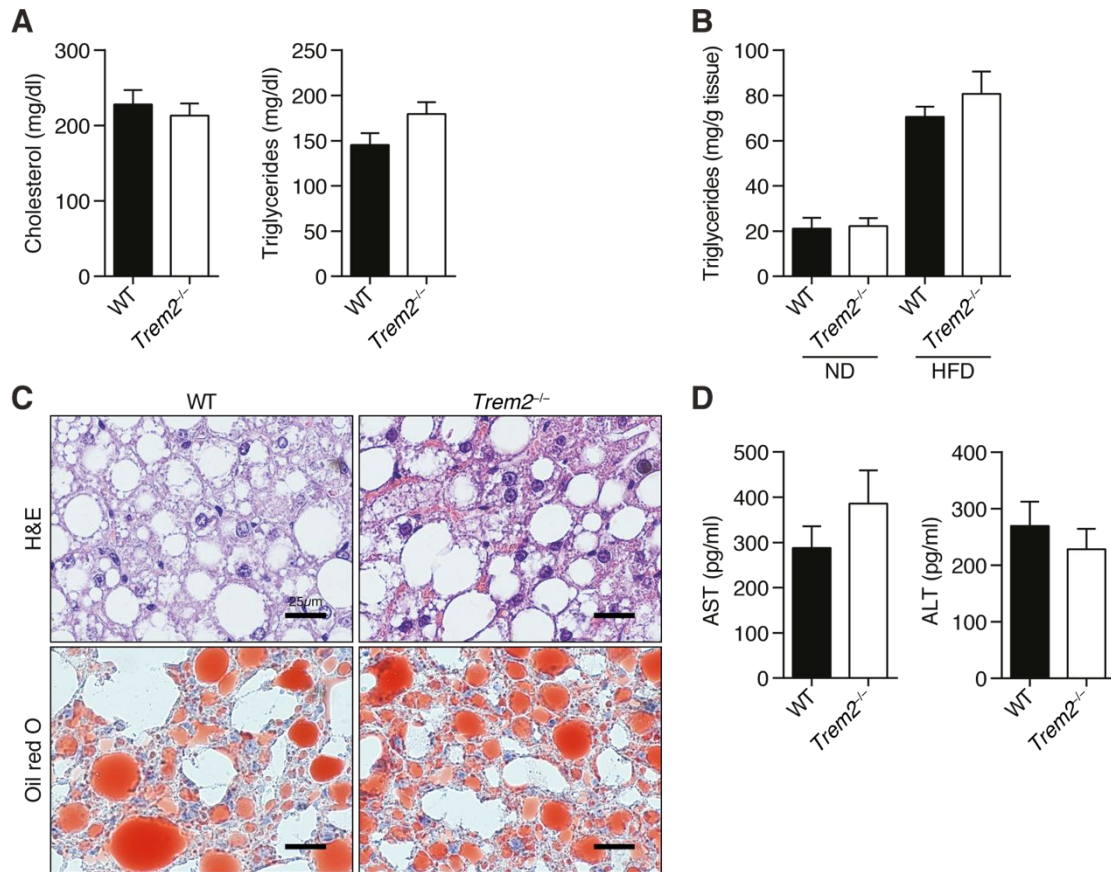
Further analysis regarding the impact of myriocin was conducted in python 3.7.9. Lipidomic values are normalized between 0 (minimum) and 1 (maximum) for each lipid individually. This type of normalization is particularly suitable for the vastly differing concentration ranges between the individual lipids. Values smaller than the limit of detection ($< \text{LOD}$) were set to zero for further calculations. When calculating group averages, lipids were first averaged before the normalization step was performed. When calculating difference between groups of experiments, \log_2 transformed fold changes were calculated.

Supplemental Figures

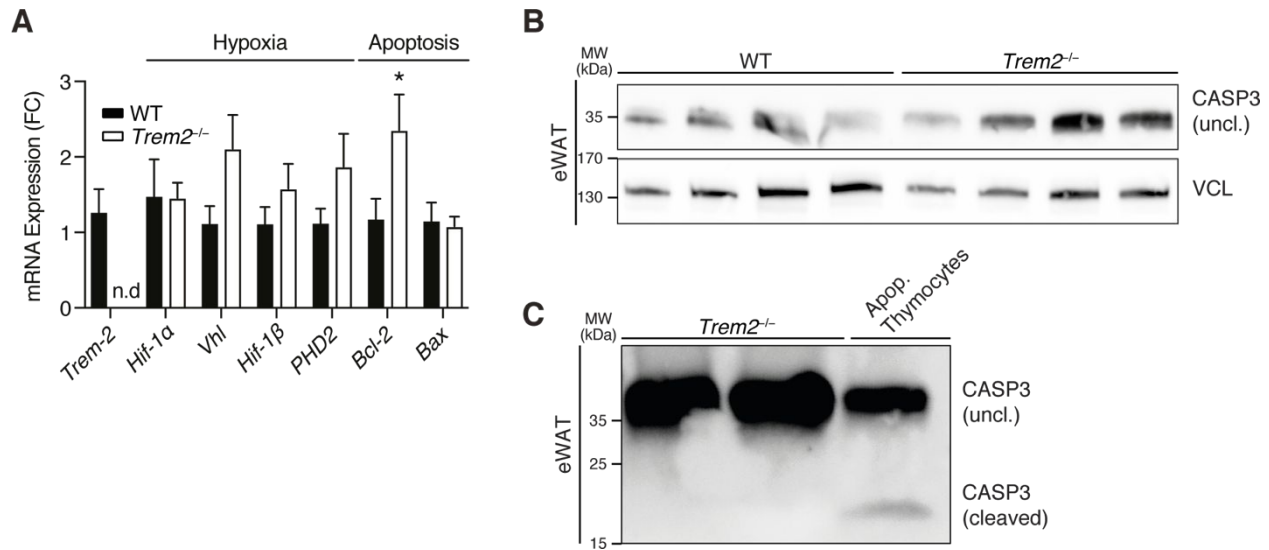


Supplemental Figure. 1 TREM2 only influences metabolic health following metabolic stress.

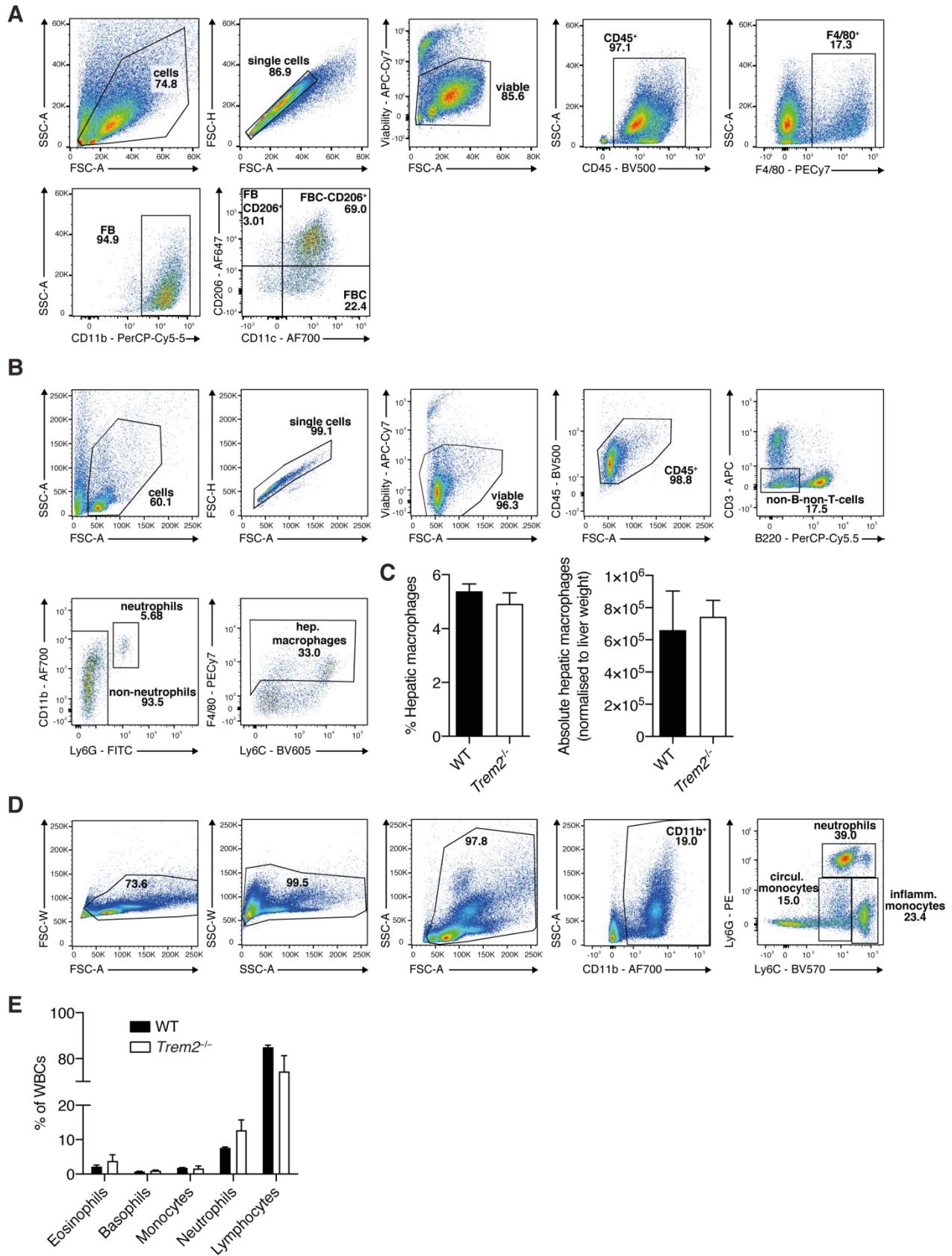
(A) Insulin tolerance test post normal chow diet (ND) or HFD at the indicated times, $n = 6-7$ mice per genotype and diet. (B) Weight curve of mice in (A). (C) Insulin tolerance test post 26 weeks ND, $n = 3-4$ mice per genotype. (D) Insulin tolerance test of 1 year old WT and *Trem2*^{-/-} mice fed a ND, $n = 4-5$ mice per genotype. Results are mean \pm SEM. Statistical analysis was performed with two-way ANOVA followed by Bonferroni post-test. * $P < 0.05$, ** $P < 0.01$, *** $P < 0.001$, **** $P < 0.0001$.



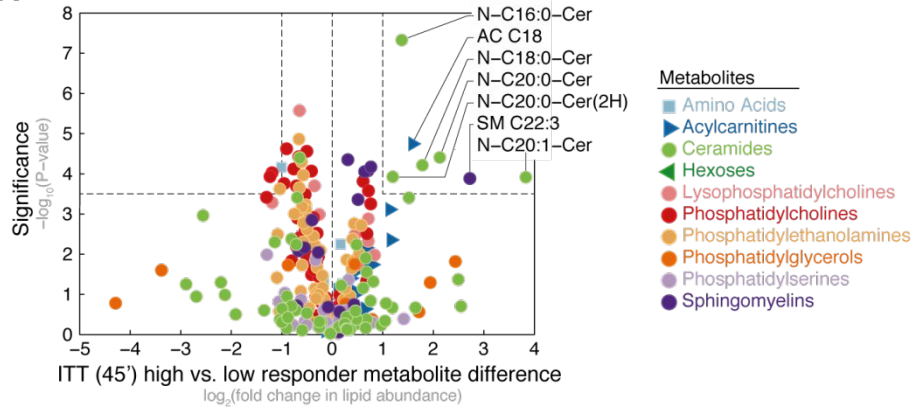
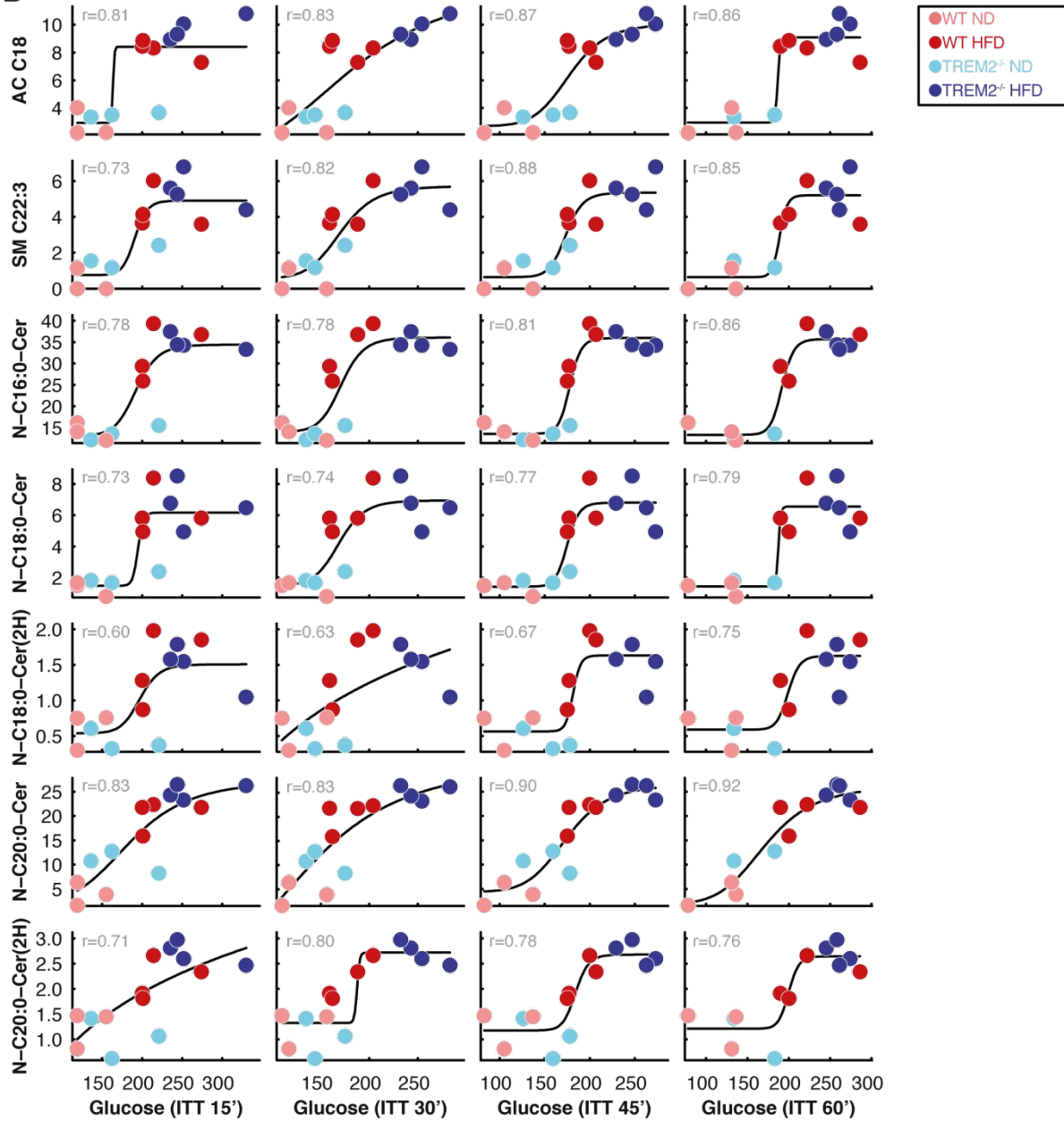
Supplemental Figure. 2 Liver and serum parameters 13 weeks post HFD. (A) Serum cholesterol and triglyceride levels of mice fed a HFD for 13 weeks, n = 7-9 mice per genotype. (B) Liver triglyceride levels of both genotypes of mice fed a normal chow diet (ND) or HFD for 13 weeks, n = 4 mice per genotype, ND and 7 mice per genotype HFD. (C) Representative liver sections (H&E, oil Red O), 13 weeks post HFD. (D) Serum levels of liver enzymes 13 weeks post HFD, n = 7-9 mice per genotype. Results are mean \pm SEM and are pooled data from 2 independent experiments.



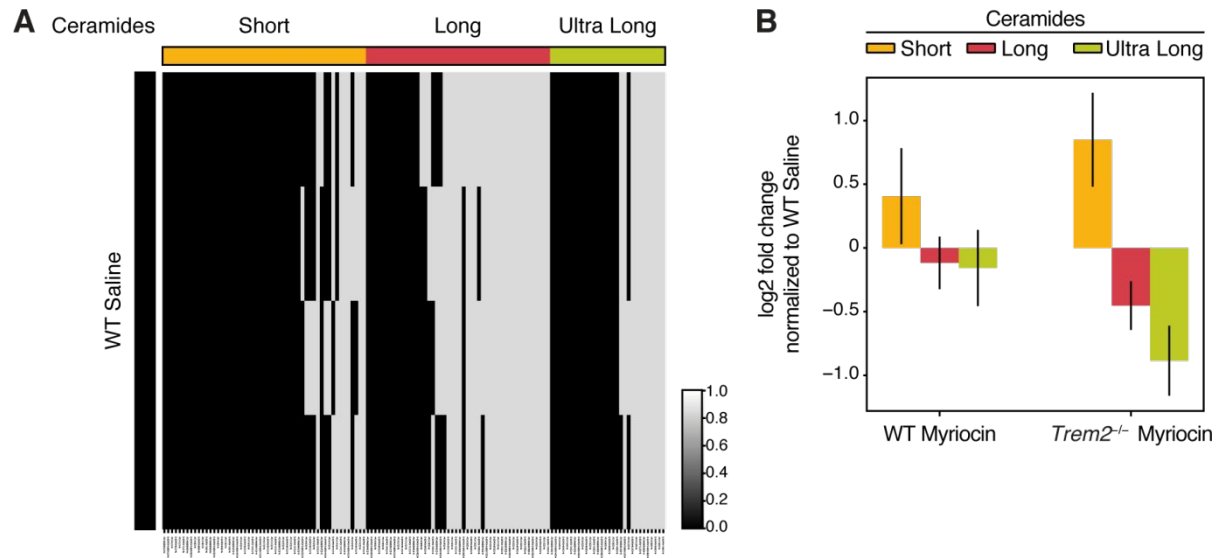
Supplemental Figure. 3 Hypoxia or apoptosis related gene expression and caspase 3 expression in epididymal white adipose 13 weeks post HFD. (A) Hypoxia and apoptosis related gene expression in epididymal white adipose (eWAT) of both genotypes fed at HFD for 13 weeks, n = 8 mice per genotype. (B) Caspase 3 western blot of eWAT of both genotypes fed a HFD for 13 weeks, n = 4 mice per genotype (C) Confirmation the caspase 3 antibody detects cleaved caspase 3 in murine apoptotic thymocytes but not in eWAT. Depicted in this blot is eWAT from two 13 week HFD fed *Trem2*^{-/-} animals. Results are mean ± SEM and in (A) are pooled from 2 independent experiments. Statistical analysis was performed with a Students t-test. * P < 0.05



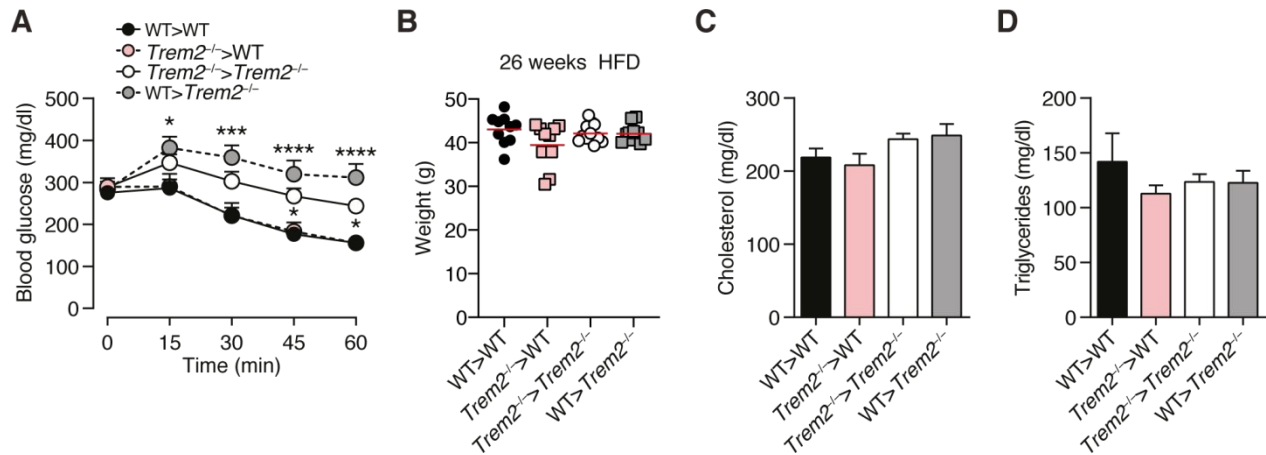
Supplemental Figure. 4 Gating strategy for adipose tissue macrophages (ATMs), hepatic macrophages and white blood cells (WBCs). Hepatic macrophage % and absolute number and white blood cell counts post 26 weeks HFD in both genotypes. (A) ATMs were defined as viable CD45⁺F4/80⁺CD11b⁺ cells and were further sub-gated for CD11c and CD206. **(B)** Hepatic macrophage gating strategy. Tissue resident liver macrophages were defined as viable CD45⁺CD3⁻B220⁻Ly6G⁻CD11b⁺Ly6C⁺F4/80⁺ cells. **(C)** Quantification of the percentage and absolute numbers of liver F4/80⁺ cells gated as in **(B)** in WT and *Trem2*^{-/-} mice fed a HFD for 26 weeks, n = 3 mice per genotype. **(D)** Gating strategy for blood monocytes and neutrophils. Neutrophils were defined as CD11b⁺Ly6G⁺, circulating monocytes as CD11b⁺Ly6C^{lo} and inflammatory monocytes as CD11b⁺Ly6C^{hi}. **(E)** White blood cells counts of obese WT and *Trem2*^{-/-} mice fed a HFD for 26 weeks, n = 3-4 mice per group.

A**B**

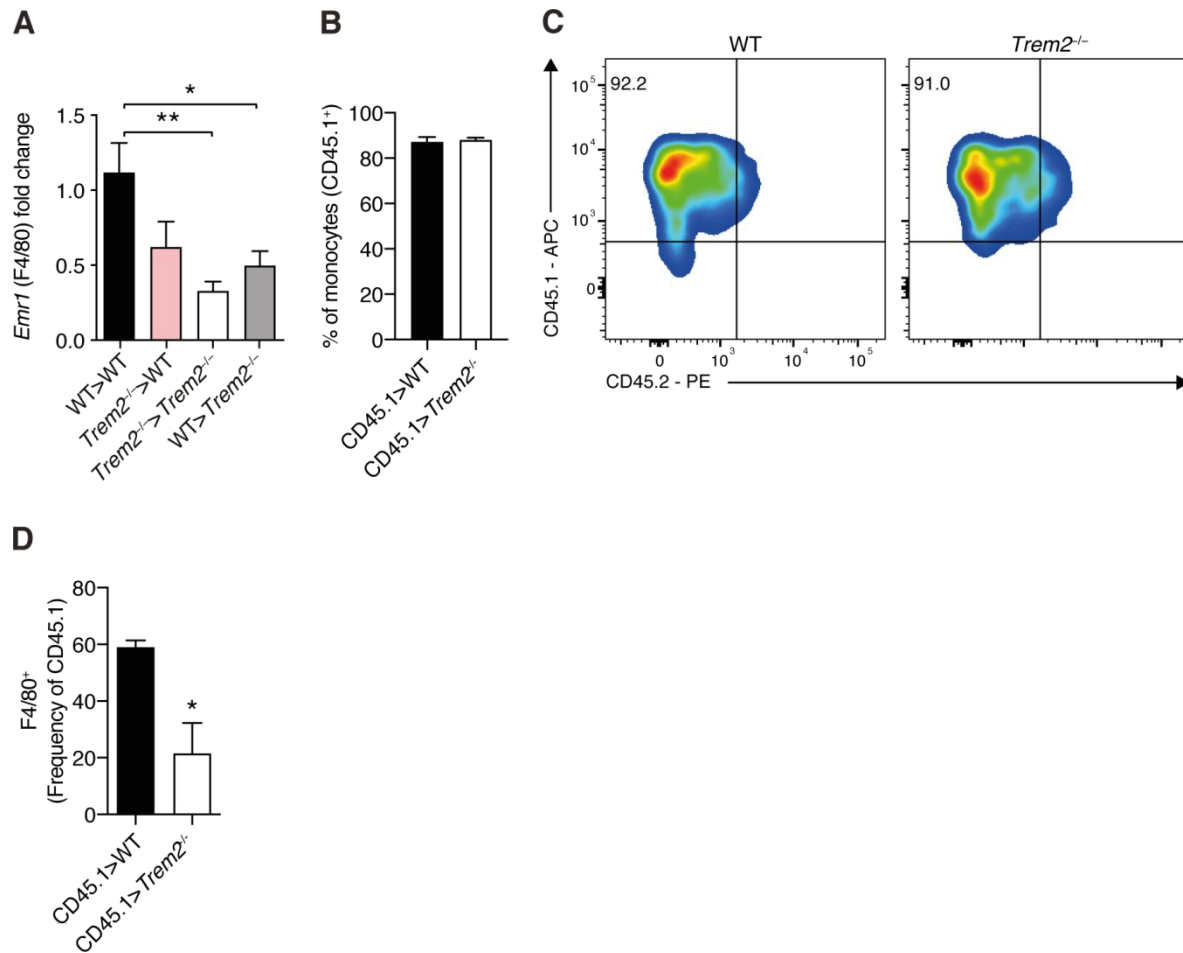
Supplemental Figure. 5 Obesity triggered synthesis of long chain ceramides is associated with hyperglycemia upon insulin treatment. (A) $\text{Log}_2(\text{FC})$ metabolite levels in the 5 mice with the highest glucose levels after 45min of insulin treatment compared to the 5 mice with the lowest levels (x-axis) plotted against the significance of the corresponding metabolite difference ($\text{log}_{10}(\text{P-value})$; y-axis). Dots represent metabolites, colored as indicated in legend. **(B)** Glucose levels (x-axis) versus relative abundance of selected lipids (y-axis) following 15, 30, 45 and 60 min of insulin challenge. Dots represent mice, colored as indicated in legend.



Supplemental Figure. 6. Reproducible upregulation of long chain ceramides 26 weeks post HFD and impact of myriocin on ceramide synthesis in both genotypes. (A) Serum levels of short ($C < 16$), long ($C16-C24$) and ultra-long ($> C24$) ceramides in 4 WT animals 26 weeks post HFD feeding. Long chain ceramides are especially prevalent. Black indicates ceramides below the detection limit and grey indicates those detected regardless of concentration. Short, long and ultra-long ceramides are depicted in yellow, red and green respectively. **(B)** Bar charts represent the average Log₂-fold change (FC) in abundance of short, long and ultra-long chained ceramides for both genotypes of myriocin treated animals compared to WT saline controls. $n = 4$ mice per condition. Results in **(B)** are mean \pm SEM.



Supplemental Figure. 7 Secondary liver steatosis of *Trem2*^{-/-} mice is independent of weight, triglyceride and cholesterol levels. (A) Insulin tolerance test of bone marrow transplanted mice 26 weeks post DIO; WT (WT>WT), *Trem2*^{-/-} (*Trem2*^{-/-}>*Trem2*^{-/-}) or chimeric mice - WT mice with *Trem2*^{-/-} bone marrow (*Trem2*^{-/-}>WT) and *Trem2*^{-/-} transplanted with WT bone marrow (WT>*Trem2*^{-/-}). **(B)** Weights of mice in (A) and Figure. 6D-H. **(C)** Serum cholesterol and triglyceride levels of mice in (A-B) and Figure. 6D-H. Data represent mean ± SEM and are pooled data from 2 independent experiments. Statistical analysis was performed with two-way ANOVA followed by Bonferroni post-test (A). n = 10-12 mice per genotype. * P < 0.05, **** P < 0.0001 and are versus WT>WT group.



Supplemental Figure. 8 BMT confirms that signals derived from TREM2 deficient adipose regulate ATM content. (A) F4/80 transcript levels in bone marrow transplanted mice 26 weeks post DIO; WT (WT>WT), *Trem2*^{-/-} (*Trem2*^{-/-}>*Trem2*^{-/-}) or chimeric mice - WT mice with *Trem2*^{-/-} bone marrow (*Trem2*^{-/-}>WT) and *Trem2*^{-/-} transplanted with WT bone marrow (WT>*Trem2*^{-/-}). (B) % of CD45.1 monocytes (defined as CD11b⁺Ly6G⁻F4/80⁻CD45.1⁺) in CD45.2 WT and *Trem2*^{-/-} mice following bone marrow transplantation (BMT) with CD45.1 bone marrow and HFD feeding for 26 weeks, n = 4 mice per group. (C) Representative FACS plot of (B). (D) Frequency of CD45.1 macrophages (defined as viable, CD45.1⁺F4/80⁺) in epididymal white adipose (eWAT) post BMT of CD45.2 WT and *Trem2*^{-/-} animals transplanted with CD45.1 bone marrow and subsequently fed a HFD for 26 weeks, n = 4 mice per group.

Supplemental Table 1. Primers used in this study.

Gene	Reference Sequence	Primer Sequence
Mouse		
<i>Adipoq</i>	NM_009605.4	(Forward) AGCATCCTGAGCCCTTTTGGTGT (Reverse) TAAGCTGGGGTCTGCCTGTCC
<i>F4/80</i>	NM_010130.4	(Forward) AAAGGGAAGGCTTTCTTCATTG (Reverse) TGACACTCATTACACCACCA
<i>Gapdh</i>	NM_008084	(Forward) GGTCGTATTGGGCGCCTGGTCACC (Reverse) CACACCCATGACGAACATGGGGGC
<i>Hprt</i>	NM_013556	(Forward) GTTAAGCAGTACAGCCCCAAAATG (Reverse) AAATCCAACAAAGTCTGGCCTGTA
<i>Trem2</i>	NM_031254	(Forward) CTGGCCTGCGTTCTCCTGA (Reverse) GGTGGAGGAGGGGAGAGCAT
<i>Tnf</i>	NM_013693	(Forward) CCACCACGCTCTTCTGTCTAC (Reverse) AGGGTCTGGGCCATAGAACT
<i>Il6</i>	NM_031168	(Forward) CAAGTCGGAGGCTTAATTACACATG (Reverse) ATTGCCATTGCACAACCTTTTTCT
<i>Il1b</i>	NM_008361	(Forward) GGACAGAATATCAACCAACAAGTGATA (Reverse) GTGTGCCGTCTTTCATTACACAG
<i>Nos2</i>	NM_010927.4	(Forward) TGAAGAAAACCCCTTGTGCT (Reverse) TTCTGTGCTGTCCCAGTGAG
<i>Hif1a</i>	NM_001313920.1	(Forward) ACCTTCATCGGAAACTCCAAAG (Reverse) ACTGTTAGGCTCAGGTGAACT
<i>Vhl</i>	NM_009507.4	(Forward) CAGCTACCGAGGTCATCTTTG (Reverse) CTGTCCATCGACATTGAGGGA
<i>Hif1b</i>	NM_009709.4	(Forward) TGTCATCCTGAAGACCAACAA (Reverse) AAGGAGCTCGTTCTCATCCA

<i>Phd2</i>	NM_053207.2	(Forward) GCCCAGTTTGCTGACATTGAAC (Reverse) CCCTCACACCTTTCTCACCTGTTAG
<i>Bcl2</i>	NM_009741.5	(Forward) CTCGTCGCTACCGTCGTGACTTCG (Reverse) CAGATGCCGGTTCAGGTA CT CAGTC
<i>Bax</i>	NM_007527.3	(Forward) AAGCTGAGCGAGTGTCTCCGGCG (Reverse) GCCACAAAGATGGTCACTGTCTGCC
Human		
<i>Gapdh</i>	NM_002046.5	(Forward) CCAAGGTCATCCATGACAAC (Reverse) TGTCATACCAGGAAATGAGC
<i>Trem2</i>	NM_018965.3	(Forward) ACGAGATCTTGCACAAGGCA (Reverse) GGTAGAGACCCGCATCATGG

Supplementary references

1. Jais A, Einwallner E, Sharif O, Gossens K, Lu TTH, Soyak SM, et al. Heme Oxygenase-1 Drives Metaflammation and Insulin Resistance in Mouse and Man. *Cell*. 2014;158(1):25-40.
2. Lindroos J, Husa J, Mitterer G, Haschemi A, Rauscher S, Haas R, et al. Human but not mouse adipogenesis is critically dependent on LMO3. *Cell Metab*. 2013;18(1):62-74.
3. Lumeng CN, Bodzin JL, and Saltiel AR. Obesity induces a phenotypic switch in adipose tissue macrophage polarization. *J Clin Invest*. 2007;117(1):175-84.
4. Sharif O, Gawish R, Warszawska JM, Martins R, Lakovits K, Hladik A, et al. The triggering receptor expressed on myeloid cells 2 inhibits complement component 1q effector mechanisms and exerts detrimental effects during pneumococcal pneumonia. *PLoS Pathog*. 2014;10(6):e1004167.
5. Carpenter AE, Jones TR, Lamprecht MR, Clarke C, Kang IH, Friman O, et al. CellProfiler: image analysis software for identifying and quantifying cell phenotypes. *Genome Biol*. 2006;7(10):R100.
6. Watarai H, Nakagawa R, Omori-Miyake M, Dashtsoodol N, and Taniguchi M. Methods for detection, isolation and culture of mouse and human invariant NKT cells. *Nat Protoc*. 2008;3(1):70-8.
7. Perugorria MJ, Esparza-Baquer A, Oakley F, Labiano I, Korosec A, Jais A, et al. Non-parenchymal TREM-2 protects the liver from immune-mediated hepatocellular damage. *Gut*. 2018.
8. Saluzzo S, Gorki AD, Rana BMJ, Martins R, Scanlon S, Starkl P, et al. First-Breath-Induced Type 2 Pathways Shape the Lung Immune Environment. *Cell Rep*. 2017;18(8):1893-905.
9. Koberlin MS, Snijder B, Heinz LX, Baumann CL, Fauster A, Vladimer GI, et al. A Conserved Circular Network of Coregulated Lipids Modulates Innate Immune Responses. *Cell*. 2015;162(1):170-83.
10. Zukunft S, Prehn C, Rohring C, Moller G, Hrabe de Angelis M, Adamski J, et al. High-throughput extraction and quantification method for targeted metabolomics in murine tissues. *Metabolomics*. 2018;14(1):18.